

1 Reply to Reviewer #3

2
3 We thank the reviewer for comments. We try to address all the Reviewer's comments and
4 criticism.

5
6 *The observations presented in this paper that show the appearance of >30 keV electrons in the*
7 *"forbidden" region during quiet times is very interesting and worthy of publications. I thank the authors for*
8 *attempting to respond to my earlier criticisms, but I remained unconvinced of their claims relating the low*
9 *L injections to dayside magnetosheath jet activity, which, through a complicated chain of events, is*
10 *supposed to enhance the low latitude electric field on the nightside. I attempt to summarize my objections*
11 *as follows.*

12
13 *As I see it, these facts are supported by the evidence presented manuscript, all of which I agree with:*

- 14 • *>30 keV electrons were observed at very low L, $L < 1.2$ during a quiet interval*
- 15 • *They were likely injected from the nightside in the 2-5 MLT region*
- 16 • *They were not associated with substorm injection/activity*
- 17 • *There were global magnetic field perturbations observed throughout the dayside magnetosphere*
18 *(GOES, THEMIS, ground mags) around the same time*
- 19 • *These global field perturbations were likely related to upstream foreshock activity/waves*
- 20 • *The field perturbations were too weak to produce radial transport of >30 keV electrons and were not the*
21 *cause of the low L injections*
- 22 • *Foreshock pulses and associated magnetosheath jets were observed on the dayside*

23
24 *These represent very interesting and intriguing observations, particularly the appearance of electrons at*
25 *very low L during quiet time.*

26 *However, it is then argued that the magnetosheath jets cause hot plasma (50 eV - 10 keV) to precipitate*
27 *into the dayside auroral region ($L = 7 - 15$) and that the jet-related magnetosheath plasma can produce*
28 *significant additional ionization and increase conductivity of the high-latitude ionosphere on the dayside. It*
29 *is then argued that this enhanced dayside conductivity enhances dayside currents in the ionosphere*
30 *which "should in turn promote generation of transient localized electric fields on the nightside and*
31 *especially in the postmidnight sector, where the conductivity is weak." I do not follow this logic and there*
32 *are no additional arguments/calculations/references to support these claims.*

33
34 Yes, we agree with the reviewer that the jet-related auroral precipitations observed by POES (~1
35 $\text{erg}/(\text{cm}^2 \text{ s})$) are not strong enough to induce a strong nightside electric field. We comment this
36 important issue in the revised manuscript:

37 *"We should point out that the scenario suffers some shortcomings. The energy flux of auroral*
38 *precipitations of ~ 1 $\text{erg}/(\text{cm}^2 \text{ s})$ was observed to be weak relative to that during substorms that*
39 *results in a relatively weak additional ionization in the dayside ionosphere. It is hard to expect*
40 *that the weak increase in the ionization can induce strong electric field of $E \sim 5 \text{mV/m}$. On the*
41 *other hand, the satellite observations are sparse in space and time and, thus, a satellite might not*
42 *catch an intense jet-related localized auroral precipitation of ~10 min duration. Hence, the*
43 *experimental information about auroral precipitations on the dayside is still incomplete. "*

44
45
46 *It is then hypothesized that "the induced nightside electric field might penetrate from high to low latitudes*
47 *(very low L shells) and results in $E \times B$ drift of electrons to lower L-shells."*

48 *I do not understand the mechanism that would allow this localized nightside electric field to penetrate*
49 *from high to low latitudes. Again, there are no additional arguments/ calculations /references to support*
50 *these claims. It is then argued that it is this electric field that produces the electron injections at very low*
51 *L.*

52
53 The origin of strong electric field at $L < 1.2$ is still totally unresolved problem. However, the
54 existence of this electric field is already accepted and widely used by the scientific society (e.g.
55 Selesnick et al., 2019). Apparently the resolving of this problem is beyond the scope of our
56 study. We can only make some assumptions. This important issue is discussed in the revised
57 manuscript:

58 “Another serious problem is the generation/penetration of electric fields in the inner
59 magnetosphere at low latitudes in the night sector, which is far from complete understanding.
60 The convection electric field of up to 2 mV/m was observed at $L > 2$ during disturbed
61 geomagnetic conditions (Califf et al., 2014; 2017). During magnetic quiet, the convection
62 electric field is apparently smaller (<0.5 mV/m). On the other hand, prompt penetrating electric
63 field in the dayside ionosphere at heights ~ 100 km was estimated of ~ 2 mV/m (Huang, 2008).
64 However, electric field at heights from 1000 to 2000 km did not measured and, thus, its value is
65 unknown. There are also no models predicting strong electric fields in the inner radiation belt
66 and below. As conjugate observations of penetrating transient electric fields are still unavailable
67 for such cases of anomalous particle transport, the exact mechanism of deep electron injections
68 cannot as yet be fully determined.”

69
70
71 *In summary, I find these final arguments regarding the last chain in the (complicated) proposed scenario*
72 *to be weak and unconvincing.*

73
74 We figure out this point in the end of the paper:

75 “Summarizing, from the experimental data available, the existing scenario cannot be supported
76 firmly. It might also be that another unknown mechanism is responsible for the FEE
77 enhancements during magnetic quiet periods. In this sense, further experimental studies and *in*
78 *situ* observations of electric fields at L -shells from 1.1 to 2 as well as of dayside auroral
79 precipitations are required.”

80
81 We also discussed these issues in Introduction (e.g., Lines 111 – 123) and Discussion.
82 We should emphasize that we consider a qualitative scenario, which is based on our previous
83 publications. Ground magnetic and radar observations showed that electric fields penetrate from
84 high to low latitudes (e.g., Huang, 2008). It should be addressed that mechanisms are currently
85 under comprehensive investigations. For example, possible mechanisms of penetration of
86 electric fields can be found in the review paper by Kikuchi and Hashimoto (2016). Recently, a
87 new mechanism of electric field penetration during northward IMF was suggested by Huang
88 (2019). Probably, a specific mechanism is needed for this particular case, but this can be a
89 subject for future studies in the case if the manuscript will be available for scientific discussions.

90
91 In our interpretation of the observations, we follow the logic that electric field and conductivity
92 are interconnected phenomena. Yet it relies on findings published in our previous papers
93 (Suvorova et al., 2016; Suvorova 2017) and other studies (e.g., Sibeck et al., 1996; Vorobjev et
94 al., 2001; Han et al., 2018; Selesnick et al., 2016, and etc.) as cited in the text. We would like to
95 hope that additional arguments or contra-arguments with model calculations will appear in future
96 studies, because the observations present challenges for current models of electric field and
97 electron injections below $L < 2$ under quiet solar wind conditions.

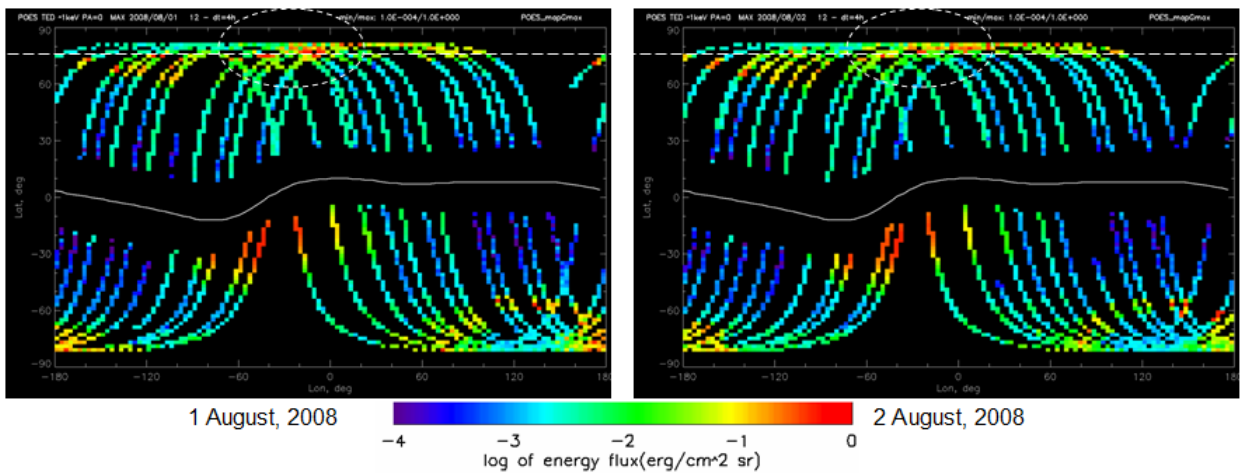
98
99 In the revised manuscript, we explain:

100 “It should be noted that most favorable conditions for FEE enhancements (and, presumably, for
101 penetration of localized electric fields) arise in the period from May to September independently
102 on geomagnetic activity level (Suvorova, 2017) Similar asymmetry in the dayside auroral
103 conductivity was also shown by Sibeck et al., (1996). Our case event on 1 August 2008
104 corresponds well to these favorable conditions. Taking into account our previous finding that the
105 occurrence of FEE enhancements is related to the ionization of the dayside ionosphere at high
106 latitudes (e.g. Suvorova, 2017), the following scenario can be considered:”

107
108
109

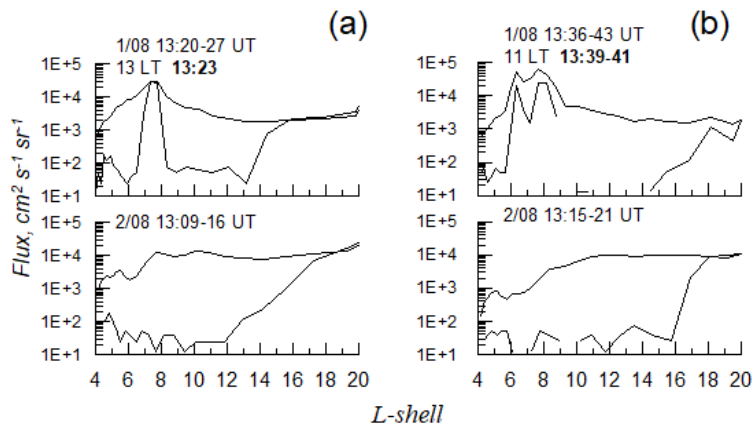
110 I will also comment that I see no relationship in Figure 11 between the magnetic field perturbations and
 111 the NOAA/POES/TED precipitation signatures.
 112 It is not demonstrated whether these TED precipitation signatures are exceptional or the norm. What do
 113 the TED measurements show before and after this interval? When the magnetic field is quiet, are these
 114 plasma precipitations observed? I suspect that the TED measurements always look like this, but one
 115 cannot be sure from the manuscript. If they are, then that begs the question why does the mechanism
 116 proposed by the authors only occur in this event, and not all of the time?
 117 What is so unique about the magnetospheric state and the observations that allow access of >30 keV
 118 electrons down to very low L values in this rare event?
 119
 120 In summary, while I think that the appearance of electrons at very low L during quiet time is a very
 121 interesting question, the authors have not convinced me that their proposed scenario is plausible, and
 122 thus I cannot recommend this article for publication.
 123

124 The main intrigue of this event is that this particular interval was accompanied by foreshock
 125 pressure pulses and by magnetosheath plasma jets. They did not occur on August 2. The hot
 126 plasma precipitations measured by the POES/TED instrument on August 1 and 2 are shown in
 127 Figure S3 (see supplement and Figure 1 below). Dayside high-latitude precipitations are marked
 128 by white circle. One can see more intense precipitations with energy flux of >0.5-1 erg/cm² sr at
 129 latitude around 76° (dashed line) and at longitude ~40°W and ~10°W during 1 August (against
 130 energy flux of <0.1 erg/cm² sr during 2 August).
 131



132
 133 **Figure 1.** Global maps of energy flux of hot plasma precipitations obtained from NOAA/POES
 134 satellites from 12 to 16 UT on 1 and 2 August 2008 (left and right, respectively). More intense
 135 precipitations with energy flux of >0.5-1 erg/cm² sr were observed at latitude around 76° (dashed
 136 line) and at longitudes ~40°W and ~10°W during 1 August (against energy flux of <0.1 erg/cm²
 137 sr during the 2 August).

138
 139 In order to demonstrate the unique magnetospheric state, we also show precipitations of >30 keV
 140 protons and electrons obtained from NOAA/POES satellites during the interval from 12 to 16
 141 UT on 1 and 2 August (see Figures S4 and S5 in supplement and Figures 2 and 3 below). In
 142 Figure 2, localized proton precipitations near noon are found at L~6-8 at 1330 UT on August 1,
 143 while they are absent on August 2.



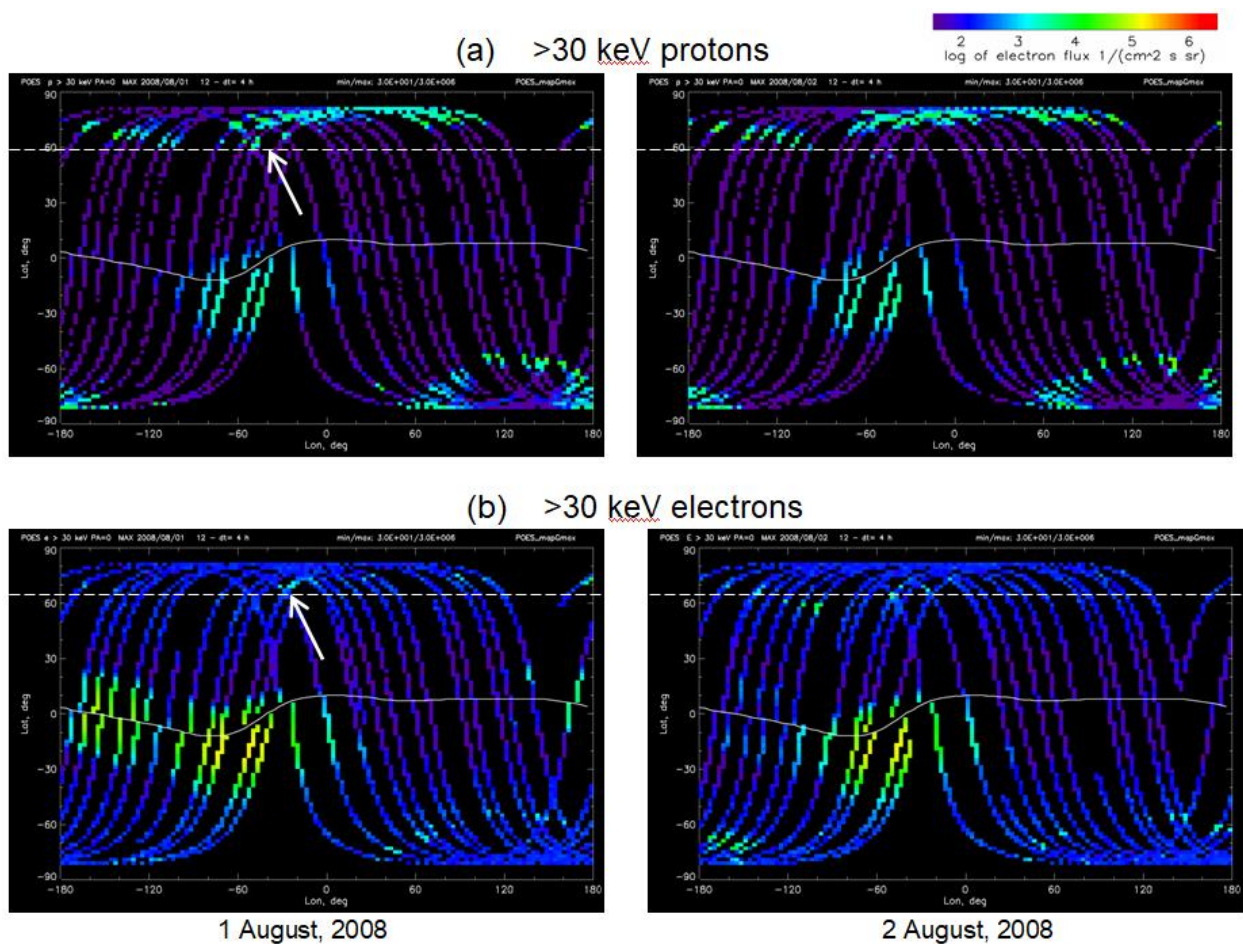
144

145 **Figure 2.** Proton fluxes with energy 30-80 keV obtained from (a) NOAA/POES-18 and (b)
 146 METOP-02 in the dayside sector on 1 and 2 August 2008. Trapped (precipitating) protons are
 147 shown by thin (thick) curves. The time moments at 13 LT and 11 LT correspond to enhanced
 148 precipitation at L~8 on August 1.

149

150 Proton and electron precipitations are shown on the global maps in Figure 3. In Figure 3a, one
 151 can see the region of intense proton fluxes around 60° of latitude (L ~ 6) within the range of 20°-
 152 80°W of longitude (near noon) on August 1, which is detached from the higher latitude
 153 “isotropic” proton fluxes associated with the plasmashield. Such detached precipitations are
 154 absent on 2 August. In other local time sectors both on August 1 and 2, precipitations occurred
 155 only in the high L-shell region (L > 14), i.e. from the plasmashield. In Figure 3b, global maps of
 156 >30 keV electron fluxes during the same interval are shown. It seems there are no features in
 157 electron precipitations on August 1 in comparison to August 2, may be except of a spot at ~20°W
 158 of longitude (marked by white arrow).

159 **Thus, there is a notable difference in the magnetospheric state during two days: in location**
 160 **and enhanced flux of the energetic particles and hot plasma precipitations in the high-**
 161 **latitude region on the dayside.**



162

163 **Figure 3.** Global maps of (a) proton fluxes with energy 30-80 keV and (b) >30 keV electron
 164 fluxes obtained from NOAA/POES satellites from 12 to 16 UT on 1 and 2 August 2008 (left and
 165 right, respectively). Proton and electron precipitations (marked by white arrows) were observed
 166 on the dayside on 1 August. There were no prominent precipitations near noon on 2 August.

167

168 Reference:

169 Huang, C.-S.: Continuous penetration of the interplanetary electric field to the equatorial
 170 ionosphere over eight hours during intense geomagnetic storms, *Journal of Geophysical*
 171 *Research*, 113, A11305, <https://doi.org/10.1029/2008JA013588>, 2008.

172 Huang, C.-S. : Global ionospheric current system associated with penetration electric field and
 173 new mechanism for the generation of dayside westward electric field at low latitudes during
 174 northward IMF. *Journal of Geophysical Research: Space Physics*, 124, 3827– 3842.
 175 <https://doi.org/10.1029/2018JA026345>, 2019.

176 Kikuchi, T., and Hashimoto, K. K.: Transmission of the electric fields to the low latitude
 177 ionosphere in the magnetosphere-ionosphere current circuit. *Geoscience Letters*, 3:4, 1-11.
 178 <https://doi.org/10.1186/s40562-016-0035-6>, 2016.

179

180

181 **Reply to Reviewer #4**

182
183 We appreciate the reviewer for very useful comments and suggestions. We add all necessary
184 clarifications in the revised manuscript and Figures in the supplement material.

185
186
187 *Suvorova et al. present an analysis of energetic electron data on August 1, 2008 at $L < 1.2$. They*
188 *report enhanced >30 keV flux during a quiet time and discussed the upstream pressure pulses as*
189 *a possible origin. The results are interesting if they are true, but the causal connection between*
190 *the pressure pulses and flux enhancements are not presented convincingly. I overall agree with*
191 *reviewer #1's concerns about the realism of the mechanism. The proposed mechanism requires*
192 *strong acceleration in the inner radiation belt, but there is no evidence that such an acceleration*
193 *is possible by small quiet-time pressure pulses. Also, when the flux enhancements were observed,*
194 *other types of magnetic activities were present, but the authors didn't check if pressure pulses*
195 *are uniquely related to the flux enhancements. M-I responses are larger in the night-dawn side*
196 *but there is no concrete demonstration of how dayside pressure pulses are causally related to*
197 *night-dawn phenomena. Specific comments are given below.*

198
199 Here we should emphasize that we consider a qualitative scenario (not a mechanism!), which is a
200 consequence of our findings published in previous papers (Suvorova et al., 2016; Suvorova
201 2017). These findings are described in details in Introduction (e.g. Lines 111 – 123). In the
202 Discussion section we explain:

203 “It should be noted that most favorable conditions for FEE enhancements (and, presumably, for
204 penetration of localized electric fields) arise in the period from May to September independently
205 on geomagnetic activity level (Suvorova, 2017) Similar asymmetry in the dayside auroral
206 conductivity was also shown by Sibeck et al., (1996). Our case event on 1 August 2008
207 corresponds well to these favorable conditions. [Taking into account our previous finding that the](#)
208 [occurrence of FEE enhancements is related to the ionization of the dayside ionosphere at high](#)
209 [latitudes \(e.g. Suvorova, 2017\), the following scenario can be considered”](#)

210
211
212 *The authors estimated that a 5 mV/m electric field is needed for the acceleration. This is an*
213 *unrealistically large number. The cited reference by Selesnick et al. [2016] concerned a storm*
214 *time event and it's not relevant for the quiet time where such a strong electric field isn't expected.*
215 *Although there is no direct observations in the inner belt for this event, the THEMIS electric field*
216 *data should be analyzed to check if such a large electric field exists. It is even more desirable to*
217 *use other events with satellites in the inner belt to demonstrate strong electric field and particle*
218 *acceleration when NOAA measures flux enhancements.*

219
220 Concerning to the electric field of 5 mV/m.

221 As we mention in the paper, there are no any experimental data about electric fields at heights
222 from 1000 to 2000 km. Hence, one can only speculate about the values. The estimation of 5
223 mV/m was obtained by Selesnick et al. (2016) in order to explain fast inward transport of
224 electrons. Our observations do not contradict to this estimation. We agree with the reviewer that
225 we do not observe this electric field. Hence, we remove the Conclusion #6.

226 Just recently, Selesnik et al. (2019) analyzed and modeled high-energy electron injections within
227 the forbidden zone. Testing models of global electrodynamics they obtained quite contradictory
228 results, which clearly showed that a large-scale storm-time electric field and electric fields in the
229 ionosphere are not sufficient in solving of this problem.

230 Hence, the electric field at $L < 1.2$ is a crucial problem not only for our study but also for all
231 other studies (see references). This problem cannot be solved up to now. Unfortunately,
232 experimental data on electric fields are restricted by $L > 2$ (Califf et al., 2014; 2017).

233 We discuss this important issue in the end of Section 3. Discussion and Summary:
234 “Another serious problem is the generation/penetration of electric fields in the inner
235 magnetosphere at low latitudes in the night sector, which is far from complete understanding.
236 The convection electric field of up to 2 mV/m was observed at $L > 2$ during disturbed
237 geomagnetic conditions (Califf et al., 2014; 2017). During magnetic quiet, the convection
238 electric field is apparently smaller (<0.5 mV/m). On the other hand, prompt penetrating electric
239 field in the dayside ionosphere at heights ~ 100 km was estimated of ~ 2 mV/m (Huang, 2008).
240 However, electric field at heights from 1000 to 2000 km did not measured and, thus, its value is
241 unknown. There are also no models predicting strong electric fields in the inner radiation belt
242 and below. As conjugate observations of penetrating transient electric fields are still unavailable
243 for such cases of anomalous particle transport, the exact mechanism of deep electron injections
244 cannot as yet be fully determined.”

245
246 Concerning to recommendation to use other events, we should explain the following:
247 This study is devoted to a unique case event of long-lasting energetic electron enhancements
248 under the IRB during very quiet geomagnetic conditions. Actually, this interval includes 8
249 independent cases of energetic electron injections under various geomagnetic and upstream
250 conditions. There are no other events of such kind when we can use THEMIS data successfully.

251
252
253 *If a strong electric field exists, other energy ranges of electrons and ions should also be*
254 *accelerated. Also, flux enhancements should occur at all L-shells. However, there is no evidence*
255 *of flux enhancements in other energies, species or L-shells. The paper needs to provide a*
256 *mechanism of how flux enhancements can occur without affecting other energies of electrons or*
257 *ions. An investigation of NOAA fluxes at higher L-shells are also needed to check if the slot*
258 *region and the outer radiation belt responded. The authors mentioned that the ring current flux*
259 *enhancements (and thus ENA flux enhancements) aren't expected. It is hard to understand why*
260 *the inner belt can respond to pressure pulses without affecting the ring current.*

261
262 Electrons with higher energies have a much shorter period of the azimuthal drift that makes
263 difficult for them to stay in the localized region of abnormal radial transport. We discussed it in
264 Lines 574-579:

265 “The multi-step process is limited by the time, during which a particle stays in the region of
266 injection. The >30 keV electrons have a long period of azimuthal drift and, thus, they can stay in
267 the region for hours. In contrast, the >100 keV electrons with the azimuthal period of ~ 6 h leave
268 quickly the injection region and, thus, do not have enough time to penetrate to the forbidden
269 zone. This effect can explain the absence of high-energy electrons in the FEE enhancements
270 presented.”

271
272 Concerning to the extension in L-shells (“An investigation of NOAA fluxes at higher L-shells are
273 also needed to check if the slot region and the outer radiation belt responded.”).

274 We clarify this important issue in the text:

275 “In the case of electric field penetrating from high to lower latitudes, the following effect might
276 be important. At higher altitudes (larger L-shells), the azimuthal drift periods of particles
277 decrease dramatically. Hence, the particles escape quickly from the localized region with the
278 enhanced electric field and, as a result, they drift earthward only a little.”

279
280 The problem of protons is discussed in Introduction:

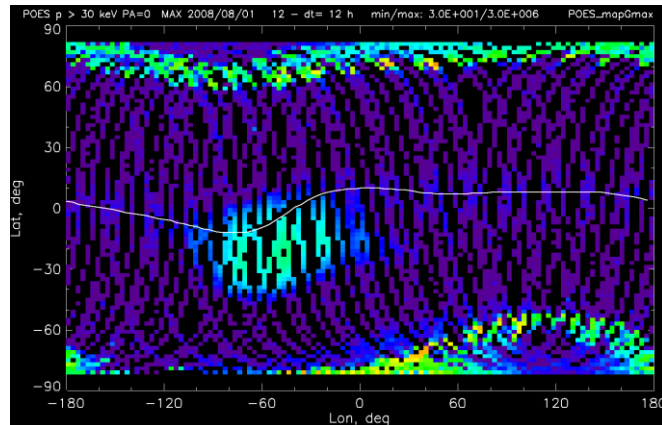
281 “From a comparison of deep penetrations of electrons and protons, Zhao et al. (2017a) have
282 revealed principle differences in these phenomena suggesting different underlying physical
283 mechanisms responsible for deep penetrations of protons and electrons. Particularly, deep proton

284 penetration is consistent with convection of plasma sheet protons, and deep electron penetration
285 suggests the existence of a local time localized mechanism.”

286

287 Concerning to the ring current problem (“*The authors mentioned that the ring current flux*
288 *enhancements (and thus ENA flux enhancements) aren't expected. It is hard to understand why*
289 *the inner belt can respond to pressure pulses without affecting the ring current.*”)

290 In the manuscript, we did not mention the “ring current” because there was no any ring current
291 at that very quiet day (see a map in Figure below). What line # of the manuscript does the
292 reviewer mean?



293

294 **Figure:** Global map of >30 keV proton fluxes measured by the detector-0 on board
295 NOAA/POES satellites on August 1, 2008 from 12 to 24 UT.

296

297

298 *The correlation between pressure pulses and flux enhancements is interesting if it is real, but it is*
299 *difficult to draw a firm conclusion from the limited event presented in this paper. The time*
300 *interval of interest includes PC index enhancements due to the southward IMF. The convection*
301 *electric field can increase under southward IMF, though it won't be as large as 5 mV/m. The*
302 *authors didn't rule out the possibilities that non-pressure-pulse effects are responsible for the*
303 *flux enhancements. It would be necessary to analyze more events to clearly show that pressure*
304 *pulses are the only cause of the flux enhancements.*

305

306 As we mention above, this event is unique. There were 8 independent injections during one quiet
307 interval. We should note that availability of observations near the dayside bow shock is crucial in
308 this type of events and such opportunity does not always exist. Fortunately, THEMIS-C was
309 located in the right place in the event presented.

310 Statistical investigation of several events will be a subject of further study. We cannot put
311 everything in one paper because it will be enormously large.

312

313 Concerning to southward IMF. Indeed, according to OMNI database (Figure 3c and 5b) IMF Bz
314 changed a sign after 1420 UT. However, a notable sharp increase of the PC index occurred at
315 ~1400 UT (Figure 3d) and, moreover, the first FEE enhancement occurred at ~1245 (Figure 2).
316 According to the THEMIS-C observations near the bow shock (Figure 5a), the southward
317 turning occurred even later, at 1550 UT. In Lines 280-284 we noted that IMF Bz was positive at
318 least until 1440 UT. The THEMIS observations convincingly prove that the PC index and FEE
319 flux enhancements during 1300-1600 UT were by no means related to southward Bz effect. On
320 the other hand, the dayside magnetospheric magnetic field pulses evidenced certainly the
321 pressure-pulse effects (Figure 6). Only based on these observations, we rule out the southward
322 IMF as a possible “non-pressure-pulse” reason for the flux enhancements in the interval 1300-
323 1600 UT.

324

325

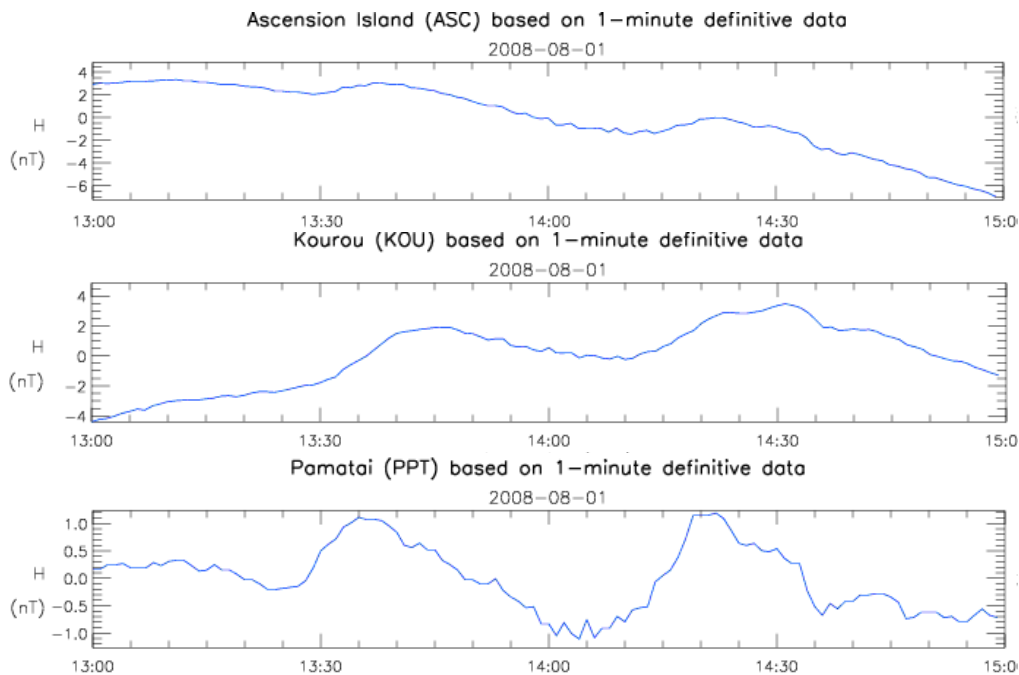
326 *Line 479: If pressure pulses cause the ground magnetic field perturbation, the largest magnetic*
327 *field signal should occur near noon, but the actual largest signal was measured near dawn. It*
328 *doesn't support the pressure pulse source but some other phenomena are more important for*
329 *creating the ground magnetic field changes.*

330

331 This is actually misinterpretation of Figure 9. It is originated from the different scaling for
332 different stations. Moreover, we did not state in the paper that “*actual largest signal was*
333 *measured near dawn*” (see Lines 479 – 480).

334 To clarify better this point, we present magnetic variations at three INTERMAGNET stations
335 during a shorter 2-h interval in Figure below. It shows the H-component of the geomagnetic field
336 at KOU, ASC and PPT from 1300 to 1500 UT. One can see that at the dayside stations KOU
337 (LT=9.5-11.5 h) and ASC (LT=12-14h) the peak-to-peak amplitude (~3-4 nT) is larger than the
338 amplitude (~2 nT) at the morning station PPT (LT=3-5 h).

339



340

341

342

343 **Figure:** A version of Figure 9 for three INTERMAGNET stations during 2-h interval from 13 to
344 15 UT. The H components of geomagnetic field at stations ASC, KOU, and PPT are shown.

345

346

347 *High-latitude magnetometer data should also be presented. Although the authors state that*
348 *substorms occur after the flux enhancement, in the equivalent current maps in the SuperMAG*
349 *website, the largest enhancements at ~13:30 UT were seen in the nightside, while angle changes*
350 *were seen in the dayside and dawnside. This plot suggests that a substorm-like nightside high-*
351 *latitude auroral activity was present. The authors should discuss how it may be related to flux*
352 *enhancements. The manuscript repeatedly mention injection, but there is no discussion about*
353 *how injection and pressure pulses are causally related. The analysis doesn't rule out the*
354 *possibility that injection is not related to pressure pulses but is caused by independent nightside*
355 *processes.*

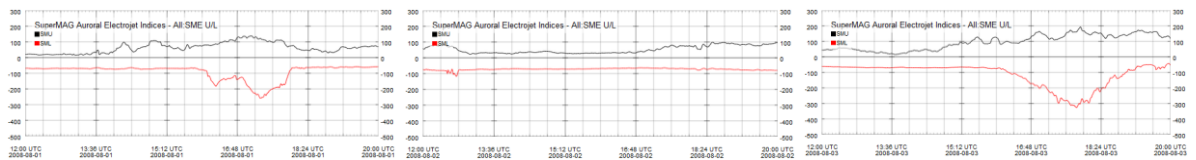
356

357 We very appreciate the Reviewer for recommendation to use the SuperMag website.

358 We compare geomagnetic activity on 1 August with that on 2 and 3 August after 1200 UT.

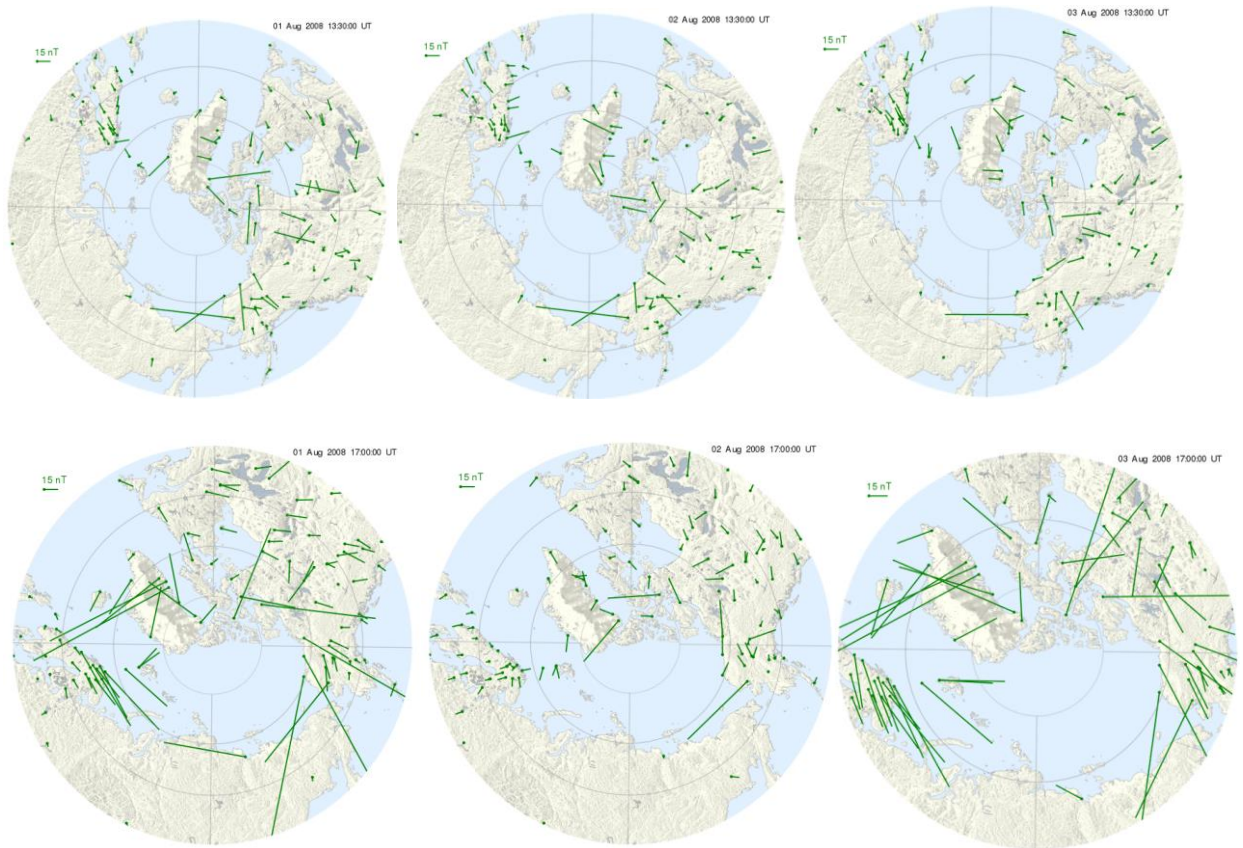
359 Corresponding geomagnetic SME indices are shown in Figure below. Geomagnetic activity in
360 the interval 12-20 UT is similar on 1 and 3 August. The quietest day is 2 August.

361



362
363
364
365
366
367
368
369
370
371
372

We have considered the magnetic data at high latitudes provided by SuperMAG website at various time intervals during 1, 2, and 3 August 2008 (see Figure below and Figure S1 in Supplement). In Figure below, we show time moments for FEE enhancements at 1330 UT (upper row) and for substorm-like event at 1700 UT (lower row). It can be clearly see that in contrast to substorm-like event (1700 UT), the high- and mid-latitude magnetic activity is weak during FEEs (1330 UT) on 1 and 3 August. This activity is comparable with the very quiet period on 2 August.



373
374

375
376

In Figure S1 (see Supplement), we show time moments at 1305, 1330, 1430 and 1540 UT during 3 days. Only one general feature can be pointed out during FEE enhancements during 13-16 UT: prominent magnetic activity in polar region at noon and in the dawn sector. This activity is definitely not related to substorms in the magnetotail but rather to the compression of the dayside magnetosphere.

382
383
384
385
386

Also, one can found that the largest enhancements in the nightside sector at all selected times during different days (even on August 2) were systematically seen at the same single station (in Alaska region). We believe that this unlikely relates to substorm-like activity. This artificial effect possibly relates to incorrect treatment of the background level at this particular station.

387
388
389
390

Concerning to substorm, we note the following in the beginning of Discussion section: “It is important to note that the intensification of AE index from 1600 to 1800 UT was originated from magnetic activity at high latitudes on the dayside (see Figure S2 in Supplement). The dayside activity results from the multiple magnetospheric compressions (see Figure 6). In this

391 context, the substorm should be rather considered as a “substorm-like” event related to
392 compressions of the dayside magnetosphere.”

393

394

395 *The peak magnetic field perturbation occurs near dawn and the authors inferred that the*
396 *injection occurred at 0-6 LT. But if upstream pressure pulses drive injection, the peak magnetic*
397 *field perturbation should be seen near noon. The authors should discuss how pressure pulses*
398 *cause nightside injection without much dayside perturbations. Nightside auroral activity could*
399 *occur without a causal connection to pressure pulses. This possibility should be discussed.*

400

401 We clarify this issue above (see the reply to comment “Line 479”). The dayside perturbations are
402 larger than nightside perturbations (see Figure in the reply). The activity was related to the
403 compression rather than to night-time substorm activity.

404

405

406 *Line 1 under radiation belt -> earthward of the inner radiation belt*

407

408 We thank the referee for the suggestion. Another alternative variant was used in the paper by
409 Selesnick et al. (JGR, 2019) “Energetic Electrons Below the Inner Radiation Belt”. One can often
410 find “under the inner radiation belt” or “below the inner radiation belt” in literature. We think
411 that both variants are appropriate.

412

413 *Line 2 nonstorm -> a nonstorm*

414 Corrected

415

416

417

418 Reference:

419 Selesnick, R. S., Su, Y.-J., & Sauvaud, J.-A. (2019). Energetic electrons below the inner
420 radiation belt. *Journal of Geophysical Research: Space Physics*, 124, 5421–5440.
421 <https://doi.org/10.1029/2019JA026718>

422 Califf, S., et al. (2014), THEMIS measurements of quasi-static electric fields in the inner
423 magnetosphere, *J. Geophys. Res. Space Physics*, 119, 9939-9951, doi:10.1002/2014JA020360.

424 Califf, S., Li, X., Zhao, et al. (2017), The role of the convection electric field in filling the slot
425 region between the inner and outer radiation belts, *J. Geophys. Res. Space Physics*, 122, 2051–
426 2068, doi:10.1002/2016JA023657.

427 Huang, C.-S. (2008). Continuous penetration of the interplanetary electric field to the equatorial
428 ionosphere over eight hours during intense geomagnetic storms, *Journal of Geophysical*
429 *Research*, 113, A11305, <https://doi.org/10.1029/2008JA013588>

430

431 **Energetic electron enhancements under radiation belt ($L < 1.2$) during a**
432 **nonstorm interval on August 1, 2008**

433 Alla V. Suvorova^{1,3}, Alexei V. Dmitriev^{2,3}, and Vladimir A. Parkhomov⁴

434 ¹ GPS Science and Application Research Center, National Central University, Jhongli, Taiwan

435 ² Institute of Space Science, National Central University, Jhongli, Taiwan

436 ³ Skobeltsyn Institute of Nuclear Physics, Lomonosov Moscow State University, Moscow,
437 Russia

438 ⁴ Baikal State University, Irkutsk, Russia

439

440 *Correspondence to:* Alla Suvorova (suvorova_alla@yahoo.com)

441 **Abstract**

442 An unusual event of deep injections of >30 keV electrons from the radiation belt to low L shells
443 ($L < 1.2$) in midnight-dawn sector was found from NOAA/POES observations during quiet
444 geomagnetic conditions on August 1, 2008. Using THEMIS observations in front of the bow
445 shock, we found transient foreshock conditions and IMF discontinuities passing the subsolar
446 region at that time. These conditions resulted in generation of plasma pressure pulses and fast
447 plasma jets observed by THEMIS, respectively, in the foreshock and magnetosheath. Signatures
448 of interactions of pressure pulses and jets with the magnetopause were found in THEMIS and
449 GOES measurements in the dayside magnetosphere and ground magnetogram records from
450 INTERMAGNET. The jets produce penetration of hot magnetosheath plasma into the dayside
451 magnetosphere as were observed by the THEMIS probes after approaching the magnetopause.
452 High-latitude precipitation of the hot plasma were observed by NOAA/POES satellites on the
453 dayside. The precipitations preceded the >30 keV electron injections at low latitudes. We propose
454 a scenario of possible association between the phenomena observed.

455

456 **Key words:** quasi-trapped energetic electrons, deep particle injections, plasma jets, subsolar
457 foreshock

458

459 **1. Introduction**

460 Deep injections of tens to hundreds of keV particles into the inner radiation belt, i.e. drift shells L
461 < 3 , during quiet or weak geomagnetic activity have recently become one of the main issues of
462 radiation belt dynamics (e.g., Park et al., 2010; Zhao and Li, 2013; Turner et al., 2017). Injection
463 or transport of particles implies violation of adiabatic motion and changing of L-shell. The cause
464 of nonstorm injections has not yet been understood.

465 The mechanisms responsible for the violation of adiabatic motion of energetic particles at low L
466 were a subject of recent studies. The studies presented some intriguing challenges for current
467 models of energetic particle injections. Observations showed that tens to hundreds of keV electrons
468 penetrate deeper than MeV energy electrons (e.g., Zhao and Li, 2013). The keV-energy electrons
469 can often penetrate down to the slot region separating the inner and outer radiation belts ($L \sim 2.5$
470 $- 3.5$) and into the inner radiation belt at $L < 2$ (e.g., Turner et al., 2017). Moreover, the deepest
471 penetrations of energetic electrons were revealed even below the inner radiation belt at $L < 1.2$
472 (Asikainen and Mursula, 2005; Suvorova et al. 2012; 2013; Dmitriev et al., 2017).

473 From a comparison of deep penetrations of electrons and protons, Zhao et al. (2017a) have revealed
474 principle differences in these phenomena suggesting different underlying physical mechanisms
475 responsible for deep penetrations of protons and electrons. Particularly, deep proton penetration is
476 consistent with convection of plasma sheet protons, and deep electron penetration suggests the
477 existence of a local time localized mechanism. Moreover, Turner et al. (2015; 2017) showed that
478 the deep injections of electrons at $L < 4$ resulted from a different mechanism than injections
479 observed at higher L shells. Particularly, Turner et al. (2015) hypothesized that the mechanism
480 could be related to wave activity in the Pi2 frequency range, which usually serves as an indicator
481 of substorm activity. Overall, dynamics of the tens to hundred keV electrons at low L -shells is
482 very different from dynamics of both protons and electrons at higher L -shells and also in higher
483 energy range. The electron injections at $L < 3$ cannot be explained by an enhanced convection

484 electric field, convection of plasma sheet electrons or inward radial diffusion (e.g., Turner et al.,
485 2017; Zhao et al., 2017a)

486 The ability of energetic electrons to penetrate deeply in the inner zone and below is still puzzling.
487 An answer to the question may be found by investigating the relation of deep injections of
488 energetic electrons to solar wind parameters, geomagnetic activity indices and other parameters of
489 magnetospheric and ionospheric responses (Suvorova, 2017; Zhao et al., 2017b). Rapid
490 enhancements of electron fluxes in the inner zone and below have been known for a long time in
491 association with strong magnetic storms (e.g., Krasovskii et al., 1961; Savenko et al., 1962; Pfitzer
492 and Winckler, 1968). However, increased statistics have revealed that deep injections of keV-
493 energy electrons may occur frequently, and furthermore, regardless of storm strength (Tadokoro
494 et al., 2007; Park et al., 2010; Zhao and Li, 2013; Suvorova et al., 2013, 2016).

495 The statistical study by Suvorova (2017) showed that electron injections into the forbidden zone
496 ($L < 1.2$) are relatively rare and occur mostly during magnetic storms and substorms. But
497 sometimes, they also occur during nonstorm conditions and weak substorm activity. This fact is
498 consistent with the recent finding of “quiet” injections in the inner radiation belt mentioned above.
499 A case of “quiet” injections of energetic electrons at $L < 1.2$ is in the focus of our study.

500 Here, we summarize the main characteristics of the electron injections into the very low L-shells
501 from several papers (Suvorova and Dmitriev, 2015; Suvorova, 2017; Dmitriev et al., 2017). The
502 quasi-trapped energetic electron population in the forbidden zone, referred to as forbidden
503 energetic electrons (FEE), can be characterized as transient with highly variable fluxes. The
504 behavior of FEE is similar to keV energy trapped electrons in the inner radiation belt with flux
505 enhancements in response to magnetic storms (e.g., Tadokoro et al., 2007; Dmitriev and Yeh,
506 2008; Zhao et al., 2017a). Simultaneous measurements of particles by satellites at different
507 altitudes provided clear evidence that the forbidden zone enhancements of energetic electrons were
508 caused by fast penetration of the inner belt electrons (Suvorova et al., 2014). As known, an
509 important role in fast transport of particles during storms is played by magnetic and electric field

510 perturbations. Such perturbations are usually associated with the influence of magnetospheric
511 substorms, or nighttime processes of magnetic field dipolarizations in the magnetotail (e.g., Glocer
512 et al., 2011). However, substorm signatures in the magnetic field in the low- L region ($L < 2$) have
513 never been observed.

514 The most probable mechanism of the FEE injections was suggested as the ExB drift (Suvorova et
515 al., 2012), and most of researchers consider and model an electric drift of inner belt electrons in
516 the ExB fields, even though the electric field must be very high (e.g., Zhao and Li, 2013; Lejosne
517 and Mozer, 2016; Selesnick et al., 2016; Su et al., 2016). According to simulation results of
518 Selesnick et al. (2016), the electric field of ~ 5 mV/m can provide deep injections at $L < 1.3$. There
519 is no explanation for penetration of a strong electric field to such low L -shells. What is more
520 important, there is no reliable information on electric fields at heights of 500-2000 km, because
521 measurements there are difficult, and, as a consequence of this, empirical electric field models are
522 limited and do not provide the results below $L \sim 2$ (e.g., Rowland and Wygant, 1998; Matsui et al.,
523 2013). The most modern research suggests that the actual strength of penetration electric fields
524 can be stronger than any existing electric field model at $L < 2$ (Su et al., 2016).

525 A relation between the FEE injections and geomagnetic activity was studied in (Suvorova et al.,
526 2013; 2014). It seemed for a while that intense geomagnetic activity like auroral substorms was
527 one of the necessary factors for deep electron injections, and the storm-time Dst -variation did not
528 control the FEE occurrences (Suvorova et al., 2014). It was suggested that substorm-associated
529 strong electric field can penetrate to the low L region, thereby creating the conditions for fast
530 earthward transport of trapped electrons in crossed E and B fields. Note that recent modeling of
531 the ExB transport mechanism at $L < 1.3$ demonstrated that the mechanism can successfully operate
532 in the low L region (Selesnick et al., 2016).

533 However, after that, many FEE events were found during moderate and weak auroral activity,
534 which was typical for pre-storm (initial phase) or even non-storm conditions and, moreover, high
535 AE index does not always guarantee injections (Suvorova and Dmitriev, 2015). Indeed,

536 statistically, such a casual relationship with substorms was not confirmed (Suvorova, 2017). From
537 total statistics of ~530 days with FEE enhancements collected during two solar cycles, more than
538 three dozen days without essential substorm activity were found. These “quiet” events occurred
539 over past decade from 2006 to 2016. The FEE enhancements in that case were observed only in
540 low energy range of tens of keV.

541 It is important to mention that one interesting feature was unexpectedly found from the statistical
542 study. It is that the most favorable conditions for the FEE enhancements arise in the period from
543 May to September independently on geomagnetic activity level. A second, minor peak of the
544 occurrence appears in the December - January period. Suvorova (2017) suggested an important
545 role of the auroral ionosphere in the occurrence of FEE injections. The peculiar annual variation
546 of the FEE occurrence rate was explained by a change in conductance of the auroral ionosphere.
547 The conductance depends directly on the illumination of the noon sector of the auroral zone. A
548 seasonal variation (summer-winter asymmetry) of dayside conductance was demonstrated by
549 Sibeck et al. (1996). As known, the high-latitude ionosphere is better illuminated during solstice
550 periods, with that the illumination of the northern region is higher than the illumination of the
551 southern one because of the dipole axis offset relative to the Earth’s center. This fact can explain
552 an existence of two peaks of the FEE occurrence with the major one during the northern summer
553 period.

554 External drivers from the solar wind should trigger some processes in the magnetosphere-
555 ionosphere system that might result in the electron injections into the forbidden zone. However,
556 the external drivers are necessary but often not sufficient for FEE enhancements to occur. If the
557 auroral ionosphere is sunlit, then impact of external drivers more likely results in the electron
558 injections into the forbidden zone. In this case, the factor of the dayside auroral ionosphere
559 conductivity is sufficient, and it comes to the fore during weak geomagnetic activity. The relevant
560 processes in the magnetosphere-ionosphere chain during magnetic quiet are still unclear. A
561 comprehensive analysis of the solar wind drivers and magnetospheric response may help us to lift

562 the veil. In this paper, we study prominent FEE enhancements during nonstorm condition on
563 August 1, 2008 in order to determine their possible drivers in the solar wind. Note that this event
564 is a subset (1%) of the total statistics collected by Suvorova (2017) during various conditions, from
565 magnetic quiet to extremely strong geomagnetic storms.

566

567 **2. Observations on August 1, 2008**

568 **2.1. Forbidden Electron Enhancements**

569 Figure 1 shows large enhancements of the >30 keV electron fluxes at low latitudes on August 1,
570 2008. The data were compiled from all orbital passes of five NOAA/POES satellites. The electron
571 fluxes in the energy ranges >30 , >100 and >300 keV were measured by the MEPED instruments
572 boarded on each satellite. The MEPED instrument includes two identical electron solid-state
573 detector telescopes and measures particle fluxes in two directions: along and perpendicular to the
574 local vertical direction (Evans and Greer, 2004). The data shown in Figure 1 are from the 0-degree
575 telescope oriented along the orbital radius-vector (i.e. vertically), so that it measured quasi-trapped
576 particles near the equator and precipitating particles in the auroral region. The forbidden zone is
577 defined as $L < 1.2$ in the longitudinal range from 0° to 260°E (or 100°W) that is beyond the South
578 Atlantic anomaly (SAA). The drift L-shells are calculated from IGRF-2005 model. Figure 1a
579 shows the observations of >30 keV electrons at 0 - 12 UT. At that time, the satellites passed the
580 same regions but they did not detect any FEE enhancements. Figure 1b shows the interval 12 - 24
581 UT, when fluxes of >30 keV quasi-trapped electrons in the forbidden zone increased by 3 orders
582 of magnitude above a background of $\sim 10^2$ ($\text{cm}^2 \text{ s sr}^{-1}$).

583 We have selected FEE enhancements with intensity $>10^3$ ($\text{cm}^2 \text{ s sr}^{-1}$). As found previously, the
584 flux enhancements at low latitudes are peculiar to the quasi-trapped energetic electrons (Suvorova
585 et al., 2012). In contrast, enhancements of electrons precipitating at low latitudes are very rare,
586 weak and short. During the event, precipitating electron fluxes in the forbidden zone did not
587 increase (not shown). Fluxes of the precipitating and quasi-trapped >100 keV electrons and >30

588 keV protons did not increase also (not shown). The quasi-trapped electrons are mirroring at heights
589 below the satellite orbit (~ 850 km) in a region of $\pm 30^\circ$ latitudes, and drift eastward with a rate of
590 17° - 19° per hour toward the SAA area, where they are lost due to scattering in the dense
591 atmosphere.

592 Figure 2 and Table 1 present main characteristics of 15 FEE enhancements detected along
593 equatorial passes of NOAA/POES satellites (P2=MetOp2, P5=NOAA-15, P6=NOAA-16,
594 P7=NOAA-17, P8=NOAA-18). The fluxes kept at the enhanced level for several hours. We
595 analyze the peak fluxes in the FEE enhancements (time, local time, longitude, and L-shell).
596 Positions of the satellite orbital planes provided a good coverage of the entire local time (LT)
597 range: 9 - 21 LT (P2 and P7), 5 - 17 LT (P5 and P6), and 2 - 14 LT (P8). The coverage allows
598 determining the injection region with uncertainty of approximately 2 h. The first FEE enhancement
599 was observed at ~ 1250 UT in Central Pacific at night time (2 LT), and the last (enhancement
600 number F15) was detected at ~ 2310 UT near the western edge of SAA at day time (17 LT). As
601 seen in Figure 2a,b, the FEE enhancements peak at minimal L-shells, i.e. at the equator. The fluxes
602 decrease quickly with growing L. This pattern corresponds to a fast radial transport (injection) of
603 electrons from the inner radiation belt. Note that pitch-angular scattering of electrons gives
604 different profiles: the fluxes should be minimal at the equator and grow with L-shell.

605 It was shown statistically that electron deep injections into the forbidden zone occur in the
606 midnight - morning sector (Suvorova, 2017). During typical geomagnetic disturbances, nighttime
607 FEE enhancements are observed shortly after local injections and near an injection site, while
608 subsequent FEE enhancements at daytime are already the result of azimuthal drift of electrons
609 injected at nighttime. Hence, the nighttime (~ 2 LT) enhancements F1 and F4 of >30 keV electron
610 fluxes indicate approximately the time of injection, respectively, at ~ 1250 and ~ 1430 UT or a little
611 bit earlier. After 1530 UT, enhancements were observed at daytime (numbers F7, F9, and F11-15)
612 and are therefore associated with drifting electrons.

613 All remaining enhancements F2, F3, F5, F6, F8 and F10 of >30 keV electron fluxes were observed
614 in the early morning (5 LT) for a long time interval of ~ 4 h that lead us to suspect that the
615 enhancements were observed near the injection site. Nevertheless, we examine the assumption
616 about drift by comparing these enhancements with the injection time for numbers 1 and 4 in Table
617 1. For the enhancements F1 and F2, 30 keV electrons injected at 1250 UT must drift $\sim 35.4^\circ$ of
618 longitude in order to reach the observing satellite P5. It takes ~ 112 min with the drift rate of $19^\circ/\text{h}$
619 for 30 keV electrons at $L \sim 1.2$. However, the observed time difference between F1 and F2 is only
620 25 min that is too short for drifting from the longitude of F1 to the longitude of F2. The
621 enhancements F1 and F3 have the longitudinal difference of 26° for 1 h that is much larger than
622 19° produced by the drift of ~ 30 keV electrons. In case of higher energy electrons (e.g., ~ 50 keV),
623 the flux should have decreased notably due to falling energy spectrum.

624 Likewise, one can infer that the enhancement F4 also did not result in the enhancements F5 and
625 F6 and certainly not in the enhancements F8 and F10. Therefore, the specific longitudinal and local
626 time distributions of the enhancements indicate multiple injections during about 4.5 h in the sector
627 of 0 - 6 LT, and the injection region was confined within 3 h of local time over central and eastern
628 Pacific. In general, these characteristic of injections are in well agreement with those found from
629 the statistics (Suvorova, 2017).

630

631 **2.2. Upstream Solar Wind Conditions**

632 An intriguing aspect of these FEE injection events is that they occurred under quiet, nonstorm
633 conditions, characterized by $Dst/SYM-H \sim 0$ nT and $AE < 100$ nT (see Figure 3). We examine
634 solar wind parameters to search for drivers inducing such deep electron injections. We focus on a
635 comparison between the solar wind parameters measured far upstream and near the bow shock and
636 on their influence on the magnetospheric magnetic field during the period of interest. Global
637 indices of geomagnetic activity and upstream solar wind from the OMNI database in GSM
638 coordinates are shown in Figure 3.

639 As seen in Figure 3, the solar wind speed and density smoothly varied around averages of 400
640 km/s and 6 to 4 cm^{-3} , respectively, that resulted in gradual change of the dynamic pressure P_d from
641 2 to 1 nPa. The interplanetary magnetic field (IMF) can be characterized as weakly disturbed by
642 small-scale structures because of chaotic variations of the magnetic field components and
643 discontinuities, particularly during the first half of the day. Also, in this period, the B_z component
644 was predominately positive. Later, there was a short interval from 1500 to 1800 UT, when IMF
645 orientation was relatively steady with a continuous negative B_z of about -2 nT. The AL index
646 increased from 16 to 18 UT with a peak of -250 nT. The 1 min $SYM-H$ index was > -10 nT
647 throughout the whole day, indicating there was no geomagnetic storm.

648 Overall, the OMNI magnetic and plasma parameters can be characterized as almost undisturbed
649 in the period of the FEE enhancements from 1200 to 2300 UT. Obviously, the weak auroral activity
650 at ~1700 UT could not result in extremely deep injections of the energetic electrons, which started
651 much earlier, around 1300 UT. Whereas, looking on the PC index, which represents magnetic
652 activity in the northern (PCN) and southern (PCS) polar caps (Troshichev et al., 1988), one can
653 see a clear disturbance, particularly in the northern polar cap, in the period from 1300 to 1530 UT.
654 But it's difficult to identify appropriate solar wind drivers for interpretation of this polar cap
655 activity.

656 This raises the question of actual solar wind characteristics at the near-Earth location during the
657 event. The FEE enhancement event under the nonstorm condition and mild, ordinary solar wind
658 properties presents intriguing challenge to current understanding of the energetic particle
659 injections, which usually are associated with intense substorm activity. From the characteristic PC-
660 index behavior, we suspect the actual solar wind parameters affecting the magnetosphere may be
661 different from those predicted by OMNI. Fortunately, the near-Earth THEMIS mission can provide
662 necessary reliable information on upstream conditions.

663

664 **2.3. THEMIS foreshock observations**

665 During the time interval from 1200 to 1800 UT, the THEMIS-C satellite (TH-C) moved from the
666 subsolar region (17.2, -0.3, -5.9 Re GSM) toward dusk (18.1, 3.4, -5.9 Re GSM) (see Figure 4).
667 From the TH-C plasma and magnetic measurements (Figure 5), we infer that the probe was located
668 upstream of the bow shock, whose average subsolar position was estimated as ~ 14.6 Re for $Pd \sim 1.5$
669 nPa (Fairfield, 1971). Figure 5a shows measurements of the THEMIS-C/FGM fluxgate
670 magnetometer in GSM coordinates with a time resolution of ~ 3 s (Auster et al., 2008) and the ion
671 spectrograms from THEMIS-C/ESA plasma instrument (McFadden et al., 2008). The ion
672 spectrogram clearly demonstrates that hot ions (~ 1 keV) are of the solar wind origin and
673 magnitudes of magnetic field components correspond to IMF components in Figure 3. The
674 magnetic field components measured in situ by TH-C are compared with those predicted by OMNI
675 and shown in Figure 5b. Also, Figure 5c presents the IMF cone angles, between the IMF vector
676 and the Earth-Sun line, for both magnetic data sets. In Figure 5d, dynamic pressure for OMNI,
677 ACE and TH-C are compared.

678 We evaluate characteristics of the upstream solar wind structures actually affecting the
679 magnetosphere during the period of the FEE enhancements. From 1100 UT to 1320 UT, three TH-
680 C magnetic components demonstrated small-amplitude variations, and the B_z component had
681 northward direction. During this time, there were discrepancies between magnetic components of
682 the TH-C and OMNI data caused mostly by time shift of ~ 10 - 15 min, so that TH-C observed
683 arrival of the solar wind structures at earlier time than that predicted by OMNI. With time
684 correction, one can achieve better consistency in the two magnetic data sets except the difference
685 in the B_x components about 1310 UT.

686 In Figure 5c, the OMNI cone angle dropped below 30° between 1330 and 1520 UT that
687 corresponded to quasi-radial IMF orientation (IMF is almost along the Earth-Sun line), whereas
688 cone angle variations detected by TH-C were very different from the OMNI data. After 1500 UT,
689 the OMNI data do not match the TH-C observation any more, even with time correction. About
690 ~ 1320 UT, ~ 1400 UT and after 1440 UT, the in-situ observation of THEMIS shows large-

691 amplitude fluctuations with duration of tens of minutes in three magnetic components and cone
692 angle (Figure 5a, c). The observed large magnetic fluctuations are ultralow-frequency (ULF)
693 waves, and they are a typical signature of the upstream region of quasi-parallel bow shocks, so-
694 called foreshock (e.g., Schwartz and Burgess, 1991). In addition, in the same time intervals, the
695 plasma spectrogram shows enhancements of suprathermal ion fluxes with energy of >10 keV
696 (upper panel in Figure 5a). This is another distinguishing signature of the foreshock, known as
697 diffuse ion population, which is always observed together with the upstream ULF waves (Gosling
698 et al., 1978; Paschmann et al., 1979). Hence, the upstream foreshock waves and diffuse ions
699 observed by TH-C in the subsolar region are associated distinctly with a radial or quasi-radial IMF
700 orientation in the undisturbed solar wind. Note, that the longest foreshock interval (1435 - 1550
701 UT) associated with the quasi-radial IMF orientation was observed by ~ 20 min later than that
702 predicted by OMNI.

703 After 1520 UT, the prediction and in-situ data mismatch greatly. The TH-C satellite observed
704 several IMF discontinuities and alternation between spiral and radial orientations of the IMF
705 vector, while the OMNI magnetic field does not change the spiral orientation from 1520 to 1740
706 UT. The foreshock returned to the subsolar region periodically and more frequently in the interval
707 1600 - 1730 UT than in the earlier period 1320 - 1440 UT. This behavior indicates the transient
708 subsolar foreshock.

709 Note, these two time intervals of frequent foreshock transitions differ in the B_z component: $B_z >$
710 0 at 1320 - 1440 UT and $B_z < 0$ at 1600-1700 UT. It's natural, that the southward B_z results in the
711 weak auroral activity during the later interval. Nevertheless, the changing direction of IMF has the
712 effect on the magnetic activity in the northern polar cap during the both interval (see the PC index
713 in Figure 1).

714 Figure 5d demonstrates large difference in solar wind dynamic pressure acquired from the TH-C
715 probe, the ACE upstream monitor and OMNI data. The ACE data are shifted by 60 min. In contrast
716 to OMNI and ACE, TH-C observed strong fast fluctuations in the dynamic pressure during

717 intervals of subsolar foreshock (see Figure 5c). Note that ACE shows in average a smaller pressure
718 than OMNI predicts, and it is more close to the TH-C observations. The fluctuations in the TH-C
719 measurements are characterized by pressure pulses, which exceed sometimes the dynamic pressure
720 from ACE (e.g., at 1320-1330, 1350, 1420, 1440, 1530 and etc.). The pulses were originated from
721 plasma density enhancements because the plasma velocity remained practically constant at that
722 time (not shown). Similar foreshock phenomenon was described by Fairfield et al. (1990).
723 Apparently, the foreshock pressure pulses were further transported by the solar wind to the
724 magnetosheath and could affect the magnetopause. Similar foreshock pressure pulses and their
725 compression effects in the magnetosphere-ionosphere were reported by Korotova et al. (2011).

726

727 **2.4. Magnetospheric magnetic field perturbations**

728 We use magnetic field and plasma measurements in the magnetosphere from the other three
729 THEMIS probes and GOES-12, GOES-10 satellites in order to examine a magnetospheric
730 response to the pressure pulses in the subsolar foreshock, which forms each time with arrival or
731 departure of magnetic flux tubes with quasi-radial IMF orientation. Positions of the TH-B, TH-D,
732 TH-E and GOES-12 satellites in the X-Y GSM plane for the period from 1200 to 1800 UT are
733 shown in Figure 4. We used the model of Lin et al. (2010) to calculate magnetopause position. The
734 OMNI data at 1600 UT are used as input data for the model. The GOES-12 and GOES-10 satellites
735 moved from morning to noon (7 - 13 LT and 8-14 LT, respectively). The TH-E and TH-D probes
736 moved outward from prenoon to postnoon, and the TH-B probe moved inward in the afternoon-
737 dusk sectors.

738 Figure 6 shows variations of the Bz component measured by the TH-E, TH-D, and TH-B probes,
739 the magnetic field strength at geosynchronous orbit (GOES-12, -10), the ion spectrogram from the
740 TH-D satellite and the SYM-H index from 1100 to 1800 UT. The THEMIS magnetic data were
741 detrended using the Tsyganenko T04 geomagnetic field model (Tsyganenko and Sitnov, 2005) and

742 IGRF-2005 model (see Figure 6b). The IGRF model describes the Earth's main magnetic field and
743 the T04 model represents magnetic fields from the magnetospheric currents.

744 As seen in Figure 6 (a, e), characteristics of magnetic field and hot plasma indicate that three
745 THEMIS probes were located inside the dayside magnetosphere, a region of strong magnetic field
746 with the magnitude ranging from 40 to 150 nT and low-density of hot (>10 keV) ions. Three
747 THEMIS probes and GOES observed significant perturbations in the magnetic field with
748 increase/decrease of order of several to tens of nT (Figure 6 a-c). After 1600 UT, the largest
749 (negative) amplitudes were observed by TH-D, which was mostly close to the magnetopause.

750 From 11 to 13 UT, one can see several increases of a few nT observed by GOES and/or THEMIS
751 at ~ 1125 , ~ 1200 , ~ 1245 and ~ 1300 UT (Figure 6b). From 1300 to 1500 UT, there are a few
752 characteristic decreases and increases with duration of 20-30 min observed by all probes. The
753 magnetic field increases correspond to magnetospheric compressions, and the decreases are
754 magnetospheric expansions (e.g., Dmitriev and Suvorova, 2012). Prominent magnetic "dimple-
755 hump" structures are indicated by dashed lines (as 1, 2, and 3) and their peaks are listed in Table
756 2. We select peak-to-peak amplitudes exceeded ~ 5 nT in the GOES data (Figure 6c). The dimple-
757 hump structures show the largest amplitudes up to 15 nT in THEMIS data (Figure 6b).

758 After 1600 UT, the TH-D probe observed fast magnetic variations. At that time, the probe was
759 approaching the magnetopause and moving ahead of the TH-E probe (see Figure 4). Note, that the
760 fast magnetic fluctuations are not always seen in SYM-H index because of a low time resolution
761 (1 min). Figure 6e presents the ion spectrogram from TH-D. One can see several short-time
762 intrusions of dense and cold plasma with spectrum typical for the magnetosheath. Moreover, at
763 ~ 1700 and 1710 UT, the magnetospheric field measured by TH-D with positive B_z suddenly
764 overturned to negative B_z for a moment that indicated a magnetosheath encounter. Time moments
765 of peaks in the magnetosheath plasma pressure are indicated by lines 4-10 in Figure 6 and listed
766 in Table 2.

767 As seen in Figures 6b-d, THEMIS magnetic observations well correlate with magnetic field
768 variation observed by GOES-12,-10 in the whole interval. Time of some magnetic peaks coincides
769 well with accuracy of 1 min (e.g., at ~1200, 1300 and 1420 UT), while others demonstrate various
770 delays of 2 - 6 min between different satellites (see Table 2). In Table 2, we also list foreshock
771 pulses related to the magnetic peaks observed in the magnetosphere (see Figure 5d). Comparing
772 the time moments of magnetic peaks and foreshock pressure pulses, we found that the latter often
773 preceded the first ones by one to few minutes.

774 As we have found, the magnetic variations associated with expansion-compression effects could
775 not be caused by the pristine solar wind pressure variations, which were gradual and small during
776 the interval (see Figures 3 and 5). The magnetic perturbations can be related to the foreshock
777 pressure pulses. Unfortunately, THEMIS was not located in the magnetosheath from 1200 to 1600
778 UT, but an analysis of the later interval (1600-1800 UT) can provide important information about
779 penetration of the foreshock pressure pulses through the magnetosheath.

780

781 **2.5. Magnetosheath plasma jets interacting with the magnetopause**

782 Figure 7 shows the magnetic field and plasma parameters observed by TH-D, TH-E and TH-C
783 during the interval 1530-1800 UT. In addition, magnetic measurements from GOES 12, IMF cone
784 angle from ACE and TH-C, and dynamic pressure from TH-C are shown. After 1530 UT, the TH-
785 D and TH-E probes have observed magnetic field increases associated with the compression effect
786 (Figure 7d). After 1600 UT, TH-D was approaching the magnetopause and started observing
787 occasionally magnetosheath plasma in the magnetosphere, as seen in the ion spectrogram (e.g.,
788 lines #4 – 7 and 10, Figures 7b). After 1700 UT, the probe twice encountered the magnetosheath
789 region as indicated by lines #8 and #9. The magnetosheath plasma can be recognized as dense and
790 cold (<1 keV) ion population.

791 As seen in Figure 7 (panels b and d), not all magnetic peaks are accompanied by plasma
792 penetrations. During the interval, the outermost probe TH-C observed occasionally the foreshock
793 phenomena, such as diffuse ions (≥ 10 keV), ULF waves and pressure pulses (panels a, e, f). As
794 one can see, most of the magnetic peaks at panel d and/or magnetosheath ions at panel b were
795 preceded by the foreshock pressure pulses within 1-5 min (panel f), for example at ~ 1549 , ~ 1611 ,
796 ~ 1625 UT and etc. (see Table 2). There are exceptions for plasma penetrations #6 at 1648 UT and
797 #7 at 1651:30 UT. Note that those events were preceded by IMF discontinuities as one can find in
798 rotation of the cone angle (panel e) at 1645 and 1650 UT, respectively.

799 Figure 8 shows characteristics of magnetosheath plasma in details for three intervals 1600-1630,
800 1630-1700, and 1658-1728 UT. Since plasma charge neutrality means equal density of ions and
801 electrons, Figure 8 presents parameters of the ion component only (panels a-d). Total pressure
802 (P_{tot}) and density (D) of the solar wind plasma measured far upstream by the ACE monitor are
803 also shown for comparison in panels (b, c). The time period from 1600 to 1630 UT is shown in
804 panels (a1-g1). The probes TH-D and TH-E observed magnetic field variation as a specific dimple-
805 hump pattern from 1609 to 1615 UT (panels f1, g1), similar to the variations indicated by lines #1
806 - #3 in the earlier interval (see Figure 6). This magnetic variation is preceded by the dimple-hump
807 variation in the foreshock pressure as observed by TH-C at 1607 to 1611 UT (see Figure 7f).

808 The dimple-hump variations are followed by penetration of the magnetosheath ions into the
809 magnetosphere as observed by TH-D at 1614 to 1616 UT (#4 in Table 2). At 1614 - 1616 UT, TH-
810 D was located in the magnetosphere but it observed cold ions (~ 100 eV - 3 keV) and electrons (< 1
811 keV, not shown) of the magnetosheath origin (Figure 8, panel a1). The plasma has maximal speed
812 of > 200 km/s and high density of $3-9$ cm $^{-3}$ that result in the high total pressure of 1.5 - 1.8 nPa
813 (panels b1-d1). Its dynamical characteristics distinctly exceed the solar wind parameters with
814 density of $4-5$ cm $^{-3}$ and total pressure of ~ 1.1 nPa (panels b1, c1). The internal structure of plasma
815 forms 3 prominent pressure pulses between 16:14:50 and 16:16:00 UT, a central pulse is
816 dominated by magnetic component (panel f1) and two lateral pulses are dominated by dense

817 plasma components (panel c1). Two plasma density enhancements produced a diamagnetic effect
818 seen as a characteristic decrease of magnetic field (panel f1). At the outer edge of the plasma
819 structure, the anti-sunward velocity ($V_x < 0$) reached high value of -100 km/s, indicating that the
820 local plasma flow struck and interacted with the magnetopause (panel d1). The V_z component
821 demonstrates a maximal value in southward direction (-200 km/s). Three rotated velocity
822 components V_x , V_y and V_z indicate that vortex-like plasma structure propagated along the
823 magnetopause toward south and dusk. This dense and high-speed plasma structure is analogous to
824 the large-scale magnetosheath plasma jet studied by Dmitriev and Suvorova (2012). The jets are
825 defined as intense localized fast ion fluxes whose kinetic energy density is several times higher
826 than that in the upstream solar wind and duration is longer than 30 sec (Dmitriev and Suvorova,
827 2015; Plaschke et al., 2018).

828 Panels (a2-g2) in Figure 8 show magnetosheath plasma penetrations #5 - #7 during the time period
829 from 1630 to 1700 UT. The plasma structures #5 and #6 (panel a2) have a short duration and are
830 characterized by extremely high density of 16 and 12 cm^{-3} , respectively, that well explain the
831 compression effects in magnetic measurements from TH-E and TH-D (panels f2, g2). Prolonged
832 plasma structure #7 has lower density of 4 - 9 cm^{-3} and did not produce a notable compression in
833 accordance with to TH-E magnetic measurements (panel g2). Note that the structure #5 was
834 preceded by a foreshock pulse observed at ~1637 UT while there were no foreshock pulses before
835 the structures #6 and #7.

836 It is important that inside each plasma structure, we reveal a dense plasma core, which is
837 characterized by enhanced speed of ~150 or ~220 km/s with a dominant V_z component (negative
838 or positive). These parameters, typical for plasma jets, formed pressure of high magnitude, which
839 exceeded the upstream solar wind pressure by 50-80 % (panel b2). The magnetosheath plasma jets
840 interacted with the magnetopause that resulted in penetration of the magnetosheath plasma into
841 the magnetosphere (Dmitriev and Suvorova, 2015). The amount of penetrated plasma can be

842 comparable with estimates of the total amount of plasma entering the dayside magnetosphere
843 (Sibeck, 1999).

844 During the last period at 1658 - 1728 UT shown in panels (a3-g3), we have an excellent opportunity
845 to examine plasma parameters in the magnetosheath region adjacent to the magnetopause. Panels
846 (a3-f3) show two cases of magnetopause distortions followed by short intervals of the
847 magnetosheath from ~1700 to 1701 UT and from 1711 to ~1715 UT. The TH-D probe at distance
848 of ~10.8 Re and ~13 LT suddenly crossed the magnetopause and moved into the magnetosheath,
849 where $B_z < 0$ (panel f3). Plasma in both magnetosheath intervals has extremely high density (~20
850 cm^{-3}) and high velocity (≤ 200 km/s). In the magnetosheath, one can see local pressure pulses
851 around ~1700 UT and ~1712 UT (lines #8 and 9). For #9 case, TH-E observed a small shallow
852 hump of the magnetic field of a few nT between two depletions at 1707 and 1715 UT (panel g3).
853 The last event (#10) shown in Figure 8c is a short penetration of magnetosheath plasma
854 accompanied by a small perturbation in the magnetospheric field observed at ~1724-1725 UT
855 (panels e3, f3). The density and pressure of this structure did not exceed the solar wind parameters
856 (panel b3-d3). Note that foreshock pressure pulses preceded by few minutes the magnetic peaks
857 and plasma structures #8, #9 and #10 as seen in Figure 7.

858 Thus, we found typical characteristics of dense and fast plasma jets in all intrusions of the
859 magnetosheath plasma into the magnetosphere and in the magnetosheath itself. Most of the
860 penetrating magnetosheath jets correspond to the foreshock pressure pulses. All jet-related plasma
861 structures caused local compression effects at the dayside. This finding raises further an interesting
862 question about spatial distribution of geomagnetic field response to the impact of foreshock
863 pressure pulses on the dayside magnetopause during very quiet geomagnetic conditions at 1300 -
864 1600 UT.

865

866 **2.6. Global ground-based magnetic variations**

867 The global dynamics of geomagnetic field perturbations was studied using 1-min magnetic data
868 provided by an INTERMAGNET of ground magnetometers ([http://www.intermagnet.org/index-](http://www.intermagnet.org/index-eng.php)
869 [eng.php](http://www.intermagnet.org/index-eng.php)). We used magnetic stations located at geomagnetic latitudes below $\sim 60^\circ$ (Table 3), where
870 a significant effect of different propagation time of MHD waves in the magnetosphere was almost
871 hidden at 1 min resolution. We grouped magnetic stations in meridional and latitudinal chains.

872 Figure 9 presents relative variations of horizontal (H) component measured at equatorial and low
873 geomagnetic latitudes (from 0° to $\sim 20^\circ$) in the interval from 1100 to 1600 UT. The stations are
874 arranged in local time from morning to postmidnight. The GOES-12 and detrended TH-D magnetic
875 data are shown at bottom. Four magnetic field pulses of different amplitudes are seen around
876 ~ 1200 , ~ 1335 - 1345 , ~ 1422 - 1430 and ~ 1545 - 1550 UT practically at all stations. The last three
877 pulses correspond to those selected from THEMIS data at ~ 1334 , ~ 1421 and 1547 - 1550 UT (#1 -
878 #3, see also Table 2). Moreover, one can see the same pattern of magnetic variation “dimple-
879 hump” in both ground-based and satellite observations. An earlier magnetic pulse of a smaller
880 amplitude at ~ 1200 UT is also seen in the GOES-12 and TH-D data.

881 It is interesting, that the magnetic pulse at 1200 UT is simultaneously (within the accuracy of ~ 1
882 min resolution) observed in all local time sectors. However, the other three enhancements were
883 observed in different LT sectors at slightly different time. The time difference varies from ~ 2 min
884 to ~ 10 min. The time delay depends on the time moment when a jet interacts with the
885 magnetopause in a given latitude-longitude sector (Dmitriev and Suvorova, 2012).

886 We draw attention to the fact that low-latitude HON and PPT stations, which were located in the
887 predawn sector (2-5 LT) from 1300 to 1500 UT, demonstrate the best coincidence (with a delay
888 of ~ 1 min) of magnetic peaks #1 and #2 with those observed by THEMIS near noon. Nighttime
889 and daytime stations (PHU, GZH, KNY, KDU, GUA, MBO, ASC, TSU, BNG, AAE, ABG)
890 observed these peaks with ~ 3 - 5 min delay. The longest delay (~ 7 min) for pulses #1 and #2 is
891 found at morning/prenoon stations KOU and VSS (~ 9 - 11 LT).

892 As we have showed above, the FEE injections (F1 - F6 in Table 1) occur from ~2 to 5 LT. So, we
893 present meridional chains of stations in the predawn and midnight sectors (Figure 10). All
894 magnetic pulses are well recognized from 0° to 60° of geomagnetic latitude. In midnight and
895 predawn sectors, the magnetic pulse at ~1200 UT peaks practically simultaneously everywhere.
896 Magnetic peak #1 around ~1333 UT was delayed by ~7 min at midlatitudes (30°-60°) in the
897 midnight sector (left panel) and by ~5 min in the predawn sector (right panel). The pulse #2 shows
898 a smaller delay (~3 min) at midlatitudes. The magnetic peak #3 at most stations in both sectors is
899 observed around ~1545 UT, that is 2 min earlier than at TH-E and 1 min later than at GOES (see
900 Table 2).

901 Thus, the ground-based magnetic observations at low and middle latitudes demonstrate similarity
902 in the magnetic variations of “dimple-hump” pattern with the satellite observations in the dayside
903 magnetosphere. It should be noted that the magnetic peaks are not regular and are characterized
904 by periodicities of tens of minutes that distinct them from magnetospheric quasi-periodic ULF
905 waves with periods 1 – 600 s. Hence, the variations observed in the geomagnetic field should result
906 from pressure pulses of the subsolar foreshock and/or magnetosheath origin.

907

908 **3. Discussion and Summary**

909 In this work, using NOAA/POES and THEMIS satellites we investigated an unusual case of deep
910 injections of >30 keV electrons at $L < 1.2$ and corresponding upstream conditions during quiet day
911 on August 1, 2008. Strong FEE enhancements with intensity of up to $\sim 10^5$ (cm² s sr)⁻¹ were
912 observed by POES above central and eastern Pacific for a long time from ~1300 to 2300 UT. With
913 analysis of longitudinal and local time distributions of the enhancements we identified a series of
914 nightside injections occurred in the sector of 2 - 5 LT during the period from ~1300 to ~1700 UT
915 (Figure 2). We found that the first 6 injections (Table 1) occurred before intensification of auroral
916 activity started at 1600 UT, and hence, cannot be related to the substorm. Two injections occurred
917 during the interval of weak auroral activity at 1600 - 1800 UT.

918 It is important to note that the intensification of AE index from 1600 to 1800 UT was originated
919 from magnetic activity at high latitudes on the dayside (see Figure S2 in Supplement). The dayside
920 activity results from the multiple magnetospheric compressions (see Figure 6). In this context, the
921 substorm should be rather considered as a “substorm-like” event related to compressions of the
922 dayside magnetosphere.

923 We found that from 11 to 18 UT the magnetosphere was not completely quiet. Prominent magnetic
924 variations on the dayside were observed by THEMIS and GOES satellites and by ground-based
925 magnetometers from INTERMAGNET network. The variations correspond to magnetospheric
926 expansions and compressions. Comparative analysis of the THEMIS, OMNI and ACE data
927 showed that the geomagnetic perturbations were not driven by the dynamic pressure of the pristine
928 solar wind. Note that significant discrepancies between the OMNI data and THEMIS near-earth
929 observations under quasi-radial IMF were reported frequently (e.g., McPherron et al., 2013;
930 Suvorova and Dmitriev, 2016). THEMIS observations show firmly that geomagnetic perturbations
931 were rather related to changes in the IMF cone angle and pressure pulses in the subsolar foreshock.

932 We demonstrated that in the magnetosheath, foreshock pressure pulses could be transformed to
933 fast and dense magnetosheath streams, so-called jets. We found that 5 out of 7 magnetosheath jets
934 were preceded by the foreshock pressure pulses. These results support well the previous findings
935 that the plasma jets are typical consequence of the foreshock dynamics and variations in the IMF
936 orientation (e.g., Fairfield et al., 1990; Lin et al., 1996; Archer et al., 2012; Dmitriev and Suvorova,
937 2012; 2015; Plaschke et al., 2018). In addition, similar effects of the foreshock pressure pulses and
938 magnetosheath jets in the magnetosphere were reported (e.g., Sibeck and Korotova, 1996;
939 Korotova et al., 2011; Heitola et al., 2012).

940 In the present case, the amplitude of magnetic variations was not very high: from a few nT at
941 ground to 15 nT at THEMIS. It should be noted that such magnetic perturbations are too weak to
942 produce deep injections of >30 keV electrons below the radiation belt. On the other hand, the
943 interaction of jets with the magnetopause can result also in penetration of the magnetosheath

944 plasma inside the dayside magnetosphere (Dmitriev and Suvorova et al., 2012, 2015). Precipitation
945 of hot magnetosheath and/or magnetospheric plasma into the dayside high-latitude ionosphere
946 can cause intensification of dayside aurorae. Vorobjev et al (2001) analyzed dayside auroral
947 transient events at latitudes equatorward of the auroral oval (below 76°). They found that the
948 dayside aurora brightening was related to localized magnetospheric compressions driven by abrupt
949 changes in the foreshock (but not by variations in the [pristine](#) solar wind dynamic pressure). Recent
950 comprehensive and statistical studies present observations of dayside aurora brightening related to
951 localized magnetopause indentations (Han et al., 2018) and caused by magnetosheath high-speed
952 jets (Wang et al., 2018). Additionally, Han et al. (2016) provided direct evidence that the source
953 of precipitating particles in the dayside aurorae was the magnetosheath plasma (sometimes mixed
954 with magnetospheric plasma). Thus, these studies showed that the jet impact is responsible for
955 transient dayside aurora, which provides enhancements in conductivity of the auroral ionosphere
956 on the dayside.

957 In order to find signatures of particle precipitations at high latitudes we conducted an additional
958 analysis of hot plasma precipitations in the auroral region at L -shells from 7 to 15 during the time
959 of interest. The energy fluxes of hot plasma (from 50 eV to 10 keV) were measured by POES/TED
960 plasma spectrometer. Figure 11 demonstrates magnetic observations of THEMIS and GOES, and
961 POES observations of the energy fluxes of auroral precipitations and FEE injections. We consider
962 intense precipitations with the threshold of $0.5 \text{ (erg cm}^{-2} \text{ s}^{-1}\text{)}$, which is several times higher than
963 the background. One can see that from 11 to 16 UT, the hot plasma precipitated mainly on the
964 dayside (12 – 16 LT) while after 16 UT, the precipitations occurred practically at all local times
965 both on the day and night sides.

966 The first FEE injection (F1) at ~ 1250 UT was preceded by several geomagnetic pulses observed
967 by GOES-12 and TH-D. The pulses were not very prominent because at that time, GOES-12 was
968 located in the morning sector and TH-D was inside the geosynchronous orbit. One can see that
969 some of pulses were accompanied by dayside auroral precipitations of the hot plasma. Note that

970 POES satellites have 100 min orbital period and, hence, they can miss some of localized
971 precipitations. On the other hand, when a jet hits the magnetopause, the magnetosheath plasma is
972 not necessarily penetrating into the dayside magnetosphere and, hence, is not precipitating at high
973 latitudes [Dmitriev and Suvorova, 2015]. Nevertheless, in Figure 11, we find two cases of
974 geomagnetic pulses followed by intense dayside precipitations of the hot plasma at 1105 UT and
975 1145 UT.

976 We can propose that the dayside precipitations at high latitudes are associated with the effect of
977 jets piercing the magnetopause. The average flux of jet-related penetrating plasma was estimated
978 as $3 \cdot 10^8 \text{ (cm}^2 \text{ s)}^{-1}$ (Dmitriev and Suvorova, 2015). This particle flux corresponds well to the energy
979 fluxes $>0.5 \text{ erg cm}^{-2} \text{ s}^{-1}$ of precipitating ions with energy of $\sim 1 \text{ keV}$ measured by POES/TED at
980 high latitudes (see Figure 11). Hence, the jet-related magnetosheath plasma can produce additional
981 ionization and increase conductivity of the high-latitude ionosphere on the dayside.

982 At the same time, FEE enhancements were observed at low latitudes. It has been found that they
983 result from anomalous earthward radial $E \times B$ drift from the inner radiation belt (Suvorova et al.,
984 2014; 2016; Selesnick et al., 2019). The drift should take a certain time dT to transport electrons
985 from the inner radiation belt edge (at L -shell $L_1 = 1.2$) to the heights of $\sim 900 \text{ km}$ (L -shell $L_2 =$
986 $1.1 \sim 1.15$):

$$987 \quad dT(\text{s}) = 6380 * (L_1 - L_2) / V_{DE} \quad (1)$$

988 where the $E \times B$ drift velocity is determined as

$$989 \quad V_{DE} = 0.032 * L^3 * E, \quad (2)$$

990 where L the average L -shell in the first approach and E is azimuthal electric field in mV/m. From
991 equations (1) and (2), we estimate that the earthward drift of energetic electron across the magnetic
992 field lines from $L = 1.2$ to $L = 1.1$ takes up to 40 min under local electric field of $\sim 5 \text{ mV/m}$. Note
993 that $E \sim 5 \text{ mV/m}$ was obtained from simulations of energetic electron injections at $L < 1.3$
994 [Selesnick et al., 2016; 2019].

995 In our case of non-storm conditions, it is hard to imagine that the strong azimuthal E can persist
996 for so long time. Previously, simulations by Su et al. (2016) have showed that it is not necessary
997 for electrons to be transported earthward all the way during a single injection. Hence, we can
998 consider a multi-step radial transport produced by a number of short pulses of E . In this case, the
999 drift from $L=1.2$ to $L=1.1$ requires two or more pulses of ~ 10 min duration that is comparable with
1000 the duration of jet-related disturbances. The multi-step process is limited by the time, during which
1001 a particle stays in the region of injection. The >30 keV electrons have a long period of azimuthal
1002 drift (~ 22 hours) and, thus, they can stay in the region for hours. In contrast, the >100 keV electrons
1003 with the azimuthal period of ~ 6 h leave quickly the injection region and, thus, do not have enough
1004 time to penetrate to the forbidden zone. This effect can explain the absence of high-energy
1005 electrons in the FEE enhancements presented. [In the case of electric field penetration from high to](#)
1006 [lower latitudes, the following effect might be important. At higher altitudes \(larger L-shells\), the](#)
1007 [azimuthal drift periods of particles decrease dramatically. Hence, the particles escape quickly from](#)
1008 [the localized region with the enhanced electric field and, as a result, they drift earthward only a](#)
1009 [little.](#)

1010 In this scenario, the first FEE injection requires a long time (\sim hour and longer) and several pulses
1011 of E in order to transport energetic electrons from undisturbed edge of the inner radiation belt to
1012 $L\sim 1.1$. Then, >30 keV electrons populate L -shells from 1.15 to 1.1 that makes possible to transport
1013 electrons to 900 km heights for a short time of ~ 10 min by one pulse of strong E . The latter pattern
1014 is applicable for the FEE injection F2. As one can see in Figure 11, each FEE injection after 13
1015 UT is preceded within <30 min by intense auroral precipitations of the hot plasma.

1016 It should be noted that most favorable conditions for FEE enhancements (and, presumably, for
1017 penetration of localized electric fields) arise in the period from May to September independently
1018 on geomagnetic activity level (Suvorova, 2017) Similar asymmetry in the dayside auroral
1019 conductivity was also shown by Sibeck et al., (1996). Our case event on 1 August 2008
1020 corresponds well to these favorable conditions. [Taking into account our previous finding that the](#)

1021 occurrence of FEE enhancements is related to the ionization of the dayside ionosphere at high
1022 latitudes (e.g., Suvorova, 2017), the following scenario can be considered:

1023 1. During quiet solar wind and geomagnetic conditions, the magnetosphere can be substantially
1024 disturbed due to transient subsolar foreshock under radial IMF.

1025 2. Subsolar foreshock pressure pulses and IMF discontinuities result in generation of fast and dense
1026 plasma jets in the magnetosheath.

1027 3. The jets interaction with the dayside magnetopause produces two distinct features in the
1028 magnetosphere: geomagnetic pulses due to the compression and magnetosheath plasma
1029 penetration.

1030 4. Precipitations of the magnetosheath plasma fluxes to the dayside high-latitude ionosphere
1031 should result in a local increase of the ionospheric conductivity and an enhancement of electric
1032 currents in the dayside ionosphere. The latter should induce transient localized electric fields on
1033 the nightside and especially in the postmidnight sector.

1034 5. We hypothesize that the induced nightside electric field might penetrate from high to low
1035 latitudes (very low L shells) and produce earthward ExB drift of energetic electrons.

1036 We should point out that the scenario suffers some shortcomings. The energy flux of auroral
1037 precipitations of $\sim 1 \text{ erg}/(\text{cm}^2 \text{ s})$ was observed to be weak relative to that during substorms that
1038 results in a relatively weak additional ionization in the dayside ionosphere. It is hard to expect that
1039 the weak increase in the ionization can induce strong electric field of $E \sim 5 \text{ mV/m}$. On the other
1040 hand, the satellite observations are sparse in space and time and, thus, a satellite might not catch
1041 an intense jet-related localized auroral precipitation of $\sim 10 \text{ min}$ duration. Hence, the experimental
1042 information about auroral precipitations on the dayside is still incomplete.

1043 Another serious problem is the generation/penetration of electric fields in the inner magnetosphere
1044 at low latitudes in the night sector, which is far from complete understanding. The convection
1045 electric field of up to 2 mV/m was observed at $L > 2$ during disturbed geomagnetic conditions

1046 (Califf et al., 2014; 2017). During magnetic quiet, the convection electric field is apparently
1047 smaller (<0.5 mV/m). On the other hand, prompt penetrating electric field in the dayside
1048 ionosphere at heights ~ 100 km was estimated of ~ 2 mV/m (Huang, 2008). However, electric field
1049 at heights from 1000 to 2000 km did not measured and, thus, its value is unknown. There are also
1050 no models predicting strong electric fields in the inner radiation belt and below. As conjugate
1051 observations of penetrating transient electric fields are still unavailable for such cases of
1052 anomalous particle transport, the exact mechanism of deep electron injections cannot as yet be
1053 fully determined.

1054 Summarizing, from the experimental data available, the existing scenario cannot be supported
1055 firmly. It might also be that another unknown mechanism is responsible for the FEE enhancements
1056 during magnetic quiet periods. In this sense, further experimental studies and *in situ* observations
1057 of electric fields at L -shells from 1.1 to 2 as well as of dayside auroral precipitations are required.

1058

Data availability.

CDAWEB (<https://cdaweb.gsfc.nasa.gov/index.html>) provide the NOAA/POES energetic particle data, THEMIS magnetic and plasma data, OMNI and ACE solar wind data. Kyoto World Data Center for Geomagnetism (<http://wdc.kugi.kyoto-u.ac.jp/index.html>) provides the geomagnetic indices. The ground magnetogram were collected from INTERMAGNET network (www.intermagnet.org).

Author contributions.

AS, AD and VP processed and analyzed experimental data on energetic particles, magnetic fields and plasma. AS found the event and designed the study. AD developed the software for treatment of the satellite data. VP analyzed ground-based magnetograms and contributed to discussion of results. AS and AD performed the whole analysis of the data, prepared figures and wrote the paper, as well as answered the referees during the evaluation process.

Competing interests.

The authors declare that they have no conflict of interest.

Acknowledgements

We thank the THEMIS team for magnetic and plasma data provided. We thank the national institutes that support magnetic observatories from INTERMAGNET. We thank Prof. O.Troshichev for providing the PC-index.

Financial support.

This research was supported by grant MOST 106-2811-M-008-050 and MOST 106-2111-M-008-030-MY3 to National Central University.

References

- Archer, M. O., Horbury, T. S., and Eastwood, J. P.: Magnetosheath pressure pulses: Generation downstream of the bow shock from solar wind discontinuities, *J. Geophys. Res.*, 117, A05228, <https://doi.org/10.1029/2011JA017468>, 2012.
- Asikainen, T., and Mursula, K.: Filling the South Atlantic anomaly by energetic electrons during a great magnetic storm, *Geophys. Res. Lett.*, 32, L16102, <https://doi.org/10.1029/2005GL023634>, 2005.
- Auster, H. U., Glassmeier, K. H., Magnes, W., Aydogar, O., Baumjohann, W., Constantinescu, D., Fischer, D., Fornacon, K. H., Georgescu, E., Harvey, P., Hillenmaier, O., Kroth, R., Ludlam, M., Narita, Y., Nakamura, R., Okrafka, K., Plaschke, F., Richter, I., Schwarzl, H., Stoll, B., Valavanoglou, A., Wiedemann, M.: The THEMIS fluxgate magnetometer, *Space Sci. Rev.*, 141(1–4), 235–264, <https://doi.org/10.1007/s11214-008-9365-9>, 2008.

Califf, S., Li, X., Blum, L., et al.: THEMIS measurements of quasi-static electric fields in the inner magnetosphere, *J. Geophys. Res. Space Physics*, 119, 9939-9951, doi:10.1002/2014JA020360, 2014.

Califf, S., Li, X., Zhao, et al.: The role of the convection electric field in filling the slot region between the inner and outer radiation belts, *J. Geophys. Res. Space Physics*, 122, 2051–2068, doi:10.1002/2016JA023657, 2017.

Dmitriev, A. V., and Suvorova, A. V.: Traveling magnetopause distortion related to a large-scale magnetosheath plasma jet: THEMIS and ground-based observations, *J. Geophys. Res.*, 117, A08217, <https://doi.org/10.1029/2011JA016861>, 2012.

Dmitriev, A. V., and Suvorova, A. V.: Large-scale jets in the magnetosheath and plasma penetration across the magnetopause: THEMIS observations, *J. Geophys. Res. Space Physics*, 120, 4423–4437, <https://doi.org/10.1002/2014JA020953>, 2015.

Dmitriev, A. V., and Yeh, H.-C.: Storm-time ionization enhancements at the topside low-latitude ionosphere, *Ann. Geophys.*, 26, 867-876, 2008.

Dmitriev, A. V., Suvorova, A.V., Klimenko, M. V., Klimenko, V. V., Ratovsky, K. G., Rakhmatulin, R. A., and Parkhomov, V. A.: Predictable and unpredictable ionospheric disturbances during St. Patrick's Day magnetic storms of 2013 and 2015 and on 8-9 March 2008, *J. Geophys. Res.: Space Physics*, 122, 2398-2432, <https://doi.org/10.1002/2016JA023260>, 2017.

Glocer, A., Fok, M.-C., Nagai, T., Tóth, G., Guild, T., and Blake, J.: Rapid rebuilding of the outer radiation belt, *J. Geophys. Res.*, 116, A09213, <https://doi.org/10.1029/2011JA016516>, 2011.

Gosling, J. T., Asbridge, J. R., Bame, S. J., Paschmann, G., and Scopke, N.: Observations of two distinct populations of bow shock ions in the upstream solar wind, *J. Geophys. Res.*, 5, 957–960, 1978.

Evans, D. S., and Greer, M. S.: Polar Orbiting Environmental Satellite Space Environment Monitor: 2. Instrument descriptions and archive data documentation. Tech. Memo. version 1.4, NOAA Space Environ. Lab., Boulder, Colo., 2004.

Fairfield, D.: Average and unusual locations of the Earth's magnetopause and bow shock, *J. Geophys. Res.*, 76(28),6700-6716, 1971.

Fairfield, D. H., W. Baumjohann, G. Paschmann, H. Luehr, and D. G. Sibeck (1990), Upstream pressure variations associated with the bow shock and their effects on the magnetosphere, *J. Geophys. Res.*, 78, 3731-3744.

Han, D.-S., Nishimura, Y., Lyons, L. R., Hu, H.Q., and Yang, H. G.: Throat aurora: The ionospheric signature of magnetosheath particles penetrating into the magnetosphere, *Geophysical Research Letters*, 43, 1819-1827, <https://doi.org/10.1002/2016GL068181>, 2016.

Han, D.-S., Liu, J.-J., Chen, X.-C., Xu, T., Li, B., Hu, Z.-J., Hu, H. Q., Yang, H. G., Fuselier, S. A., and Pollock, C.J.: Direct evidence for throat aurora being the ionospheric signature of magnetopause transient and reflecting localized magnetopause indentations. *J. Geophys. Res. Space Physics*, 123, 2658-2667, <https://doi.org/10.1002/2017JA024945>, 2018.

Hietala H., N. Partamies, T. V. Laitinen, et al.: Supersonic subsolar magnetosheath jets and their effect: from the solar wind to the ionospheric convection, *Ann. Geophys.*, 30, 33-48, 2012.

Huang, C.-S.: Continuous penetration of the interplanetary electric field to the equatorial ionosphere over eight hours during intense geomagnetic storms, *Journal of Geophysical Research*, 113, A11305, <https://doi.org/10.1029/2008JA013588>, 2008.

- Korotova, G. I., D. G. Sibeck, A. Weatherwax, V. Angelopoulos, and V. Styazhkin (2011), THEMIS observations of a transient event at the magnetopause, *J. Geophys. Res.*, 116, A07224, doi:10.1029/2011JA016606.
- Krasovskii, V. I., Shklovski, I. S., Galperin, Yu. I., Svetlitskii, E. M., Kushnir, Yu. M., and Bordovskii, G. A.: The detection of electrons with energies of approximately 10 keV in the upper atmosphere (in Russian). *Iskusstvennye Sputniki Zemli*, 6, 113-126, (English translation: *Planet. Space Sci.*, 9, 27-40, 1962), 1961.
- Lejosne, S., and Mozer, F. S.: Typical values of the electric drift $E \times B/B^2$ in the inner radiation belt and slot region as determined from Van Allen Probe measurements, *J. Geophys. Res. Space Physics*, 121, 12,014–12,024, <https://doi.org/10.1002/2016JA023613>, 2016.
- Lin, Y., Lee, L. C., and Yan, M.: Generation of dynamic pressure pulses downstream of the bow shock by variations in the interplanetary magnetic field orientation, *J. Geophys. Res.*, 101, 479–493, 1996.
- Lin, R. L., Zhang, X. X., Liu, S. Q., Wang, Y. L., and Gong, J. C.: A three-dimensional asymmetric magnetopause model. *J. Geophys. Res.*, 115, A04207, <https://doi.org/10.1029/2009JA014235>, 2010.
- Matsui, H., Torbert, R. B., Spence, H. E., Khotyaintsev, Yu. V., and Lindqvist, P.-A.: Revision of empirical electric field modeling in the inner magnetosphere using Cluster data, *J. Geophys. Res. Space Physics*, 118, 4119–4134, <https://doi.org/10.1002/jgra.50373>, 2013.
- McFadden, J. P., Carlson, C. W., Larson, D., Ludlam, M., Abiad, R., Elliott, B., Turin, P., Marckwordt, M., and Angelopoulos, V.: The THEMIS ESA plasma instrument and in-flight calibration, *Space Sci. Rev.*, 141, 277–302, <https://doi.org/10.1007/s11214-008-9440-2>, 2008.
- McPherron, R. L., Baker, D. N., Pulkkinen, T. I., Hsu, T. S., Kissinger, J., and Chu, X.: Changes in solar wind–magnetosphere coupling with solar cycle, season, and time relative to stream interface, *J. Atmos. Sol. Terr. Phys.*, 99, 1-13, <https://doi.org/10.1016/j.jastp.2012.09.003>, 2013.
- Park J., Min, K. W., Summers, D., Hwang, J., Kim, H. J., Horne, R. B., Kirsch, P., Yumoto, K., Uozumi, T., Lühr, H., and Green, J.: Non-stormtime injection of energetic particles into the slot region between Earth’s inner and outer electron radiation belts as observed by STSAT-1 and NOAA-POES, *Geophys. Res. Lett.*, 37, L16102, <https://doi.org/10.1029/2010GL043989>, 2010.
- Paschmann, G., Sckopke, N., Bame, N., Gosling, J.T., Russell, C.T., and Greenstadt, E.W.: Association of low-frequency waves with suprathermal ions in the upstream solar wind, *Geophys. Res. Lett.*, 6, 209-212, 1979.
- Pfizer, K. A., and Winckler, J. R.: Experimental observation of a large addition to the electron inner radiation belt after a solar flare event, *J. Geophys. Res.*, 73(17), 5792–5797, 1968.
- Plaschke, F., Hietala, H., Archer M., et al.: Jets downstream of collisionless shocks, *Space Science Review*, 214:81, <https://doi.org/10.1007/s11214-018-0516-3>, 2018
- Rowland, D. E., and Wygant, J. R.: Dependence of the large-scale, inner magnetospheric electric field on geomagnetic activity, *J. Geophys. Res.*, 103(A7), 14959-24964, 1998.
- Savenko, I. A., Shavrin, P. I., and Pisarenko, N. F.: Soft particle radiation at an altitude of 320 km in the latitudes near the equator (in Russian). *Iskusstvennye Sputniki Zemli*, 13, 75-80 (English translation: *Planet. Space Sci.*, 11, 431-436, 1963), 1962.
- Schwartz, S. J., and Burgess, D.: Quasi-parallel shocks: A patchwork of three-dimensional structures, *Geophys. Res. Lett.*, 18, 373-376, 1991.

- Selesnick, R. S., Su, Y.-J., and Blake, J. B.: Control of the innermost electron radiation belt by large-scale electric fields, *J. Geophys. Res. Space Physics*, 121, 8417–8427, <https://doi.org/10.1002/2016JA022973>, 2016.
- Selesnick, R. S., Su, Y.-J., & Sauvaud, J.-A. (2019). Energetic electrons below the inner radiation belt. *Journal of Geophysical Research: Space Physics*, 124, 5421–5440. <https://doi.org/10.1029/2019JA026718>
- Sibeck, D. G.: Plasma transfer processes at the magnetopause, *Space Sci. Rev.*, 88, 207–283, <https://doi.org/10.1023/a:1005255801425>, 1999.
- Sibeck D.G., & G.I. Korotova (1996), Occurrence patterns for transient magnetic field signatures at high latitudes. *J. Geophys. Res.* 101, 13413–13428.
- Sibeck, D., Greenwald R.A., Bristow W.A., and Korotova G.I.: Concerning possible effects of ionospheric conductivity upon the occurrence patterns of impulsive events in high-latitude ground magnetograms, *J. Geophys. Res.*, 101(A6), 13407–13412, doi:10.1029/96JA00072., 1996
- Su, Y.-J., Selesnick, R. S., and Blake J. B.: Formation of the inner electron radiation belt by enhanced large-scale electric fields, *J. Geophys. Res. Space Physics*, 121, 8508–8522, <https://doi.org/10.1002/2016JA022881>, 2016.
- Suvorova, A. V., and Dmitriev, A. V.: Radiation aspects of geomagnetic storm impact below the radiation belt, In V. P. Banks (Ed.), *Cyclonic and Geomagnetic Storms: Predicting Factors, Formation and Environmental Impacts*, (pp. 19-75), New York: NOVA Science Publishers, Inc., 2015.
- Suvorova, A. V., and Dmitriev, A. V.: On magnetopause inflation under radial IMF, *Adv. Space Res.*, 58, 249-256, 2016.
- Suvorova, A. V., Dmitriev, A.V., and Tsai, L.-C.: On relation between mid-latitude ionospheric ionization and quasi-trapped energetic electrons during 15 December 2006 magnetic storm, *Planet. Space Sci.*, 60, 363-369, <https://doi.org/10.1016/j.pss.2011.11.001>, 2012.
- Suvorova, A. V., Dmitriev, A. V., Tsai, L.-C., Kunitsyn, V. E., Andreeva, E. S., Nesterov, I. A., and Lazutin, L. L.: TEC evidence for near-equatorial energy deposition by 30 keV electrons in the topside ionosphere, *J. Geophys. Res.*, 118, 4672–4695, <https://doi.org/10.1002/jgra.50439>, 2013.
- Suvorova, A. V., Huang, C.-M., Matsumoto, H., Dmitriev, A. V., Kunitsyn, V. E., Andreeva, E. S., Nesterov, I. A., and Tsai, L.-C.: Low-latitude ionospheric effects of energetic electrons during a recurrent magnetic storm, *J. Geophys. Res. Space Physics*, 119, 9283-9303, <https://doi.org/10.1002/2014JA020349>, 2014.
- Suvorova, A. V., Huang, C.-M., Dmitriev, A. V., Kunitsyn, V. E., Andreeva, E. S., Nesterov, I. A., Klimenko, M. V., Klimenko, V. V., and Tumanova, Yu. S.: Effects of ionizing energetic electrons and plasma transport in the ionosphere during the initial phase of the December 2006 magnetic storm, *J. Geophys Res.: Space Physics*, 121, 5880-5896, <https://doi.org/10.1002/2016JA022622>, 2016.
- Suvorova, A.V.: Flux enhancements of >30 keV electrons at low drift shells $L < 1.2$ during last solar cycles, *J. Geophys Res.: Space Physics*, 122, 12274-12287, <https://doi.org/10.1002/2017JA024556>, 2017.
- Tadokoro, H., Tsuchiya, F., Miyoshi, Y., Misawa, H., Morioka, A., and Evans, D. S.: Electron flux enhancement in the inner radiation belt during moderate magnetic storms, *Ann. Geophys.*, 25, 1359-1364, 2007.

- Tsyganenko, N. A., and Sitnov, M. I.: Modeling the dynamics of the inner magnetosphere during strong geomagnetic storms, *J. Geophys. Res.*, 110, A03208, <https://doi.org/10.1029/2004JA010798>, 2005.
- Troshichev, O. A., Andrezen, V. G., Vennerstrøm, S., and Friis-Christensen, E.: Magnetic activity in the polar cap – A new index, *Planet. Space Sci.*, 36(11), 1095–1102, 1988.
- Turner, D. L., Claudepierre, S. G., Fennell, J. F., O'Brien, T. P., Blake, J. B., Lemon, C., Gkioulidou, M., Takahashi, K., Reeves, G. D., Thaller, S., Breneman, A., Wygant, J. R., Li, W., Runov, A., and Angelopoulos, V.: Energetic electron injections deep into the inner magnetosphere associated with substorm activity, *Geophys. Res. Lett.*, 42, 2079–2087, <https://doi.org/10.1002/2015GL063225>, 2015.
- Turner, D. L., O'Brien, T.P., Fennell, J.F., Claudepierre, S. G., Blake, J. B., Jaynes, A. N., Baker, D. N., Kanekal, S., Gkioulidou, M., Henderson, M. G., and Reeves, G. D.: Investigating the source of near-relativistics and relativistics electrons in Earth's inner radiation belt, *J. Geophys. Res. Space Physics*, 122, 695–710, <https://doi.org/10.1002/2016JA023600>, 2017.
- Vorobjev, V. G., Yagodkina, O. I., Sibeck, D. G., Liou, K., and Meng, C.-I.: Polar UVI observations of dayside auroral transient events, *J. Geophys. Res.*, 106, 28,897–28,911, [doi:10.1029/2000JA000396](https://doi.org/10.1029/2000JA000396), 2001.
- Zhao, H., and Li, X.: Modeling energetic electron penetration into the slot region and inner radiation belt, *J. Geophys. Res. Space Physics*, 118, 6936–6945, <https://doi.org/10.1002/2013JA019240>, 2013.
- Zhao, H., Li, X., Baker, D.N., Claudepierre, S.G., Fennell, J. F., Blake, J. B., Larsen, B. A., Skoug, R. M., Funsten, H. O., Friedel, R. H. W., Reeves, G. D., Spence, H. E., Mitchell, D. G., and Lanzerotti, L. J.: Ring current electron dynamics during geomagnetic storms based on the Van Allen Probes measurements, *J. Geophys. Res. Space Physics*, 121, 3333–3346, <https://doi.org/10.1002/2016JA022358>, 2016.
- Zhao, H., Baker, D.N., Califf, S., Li, X., Jaynes, A. N., Leonard, T., Kanekal, S. G., Blake, J. B., Fennell, J. F., Claudepierre, S. G., Turner, D. L., Reeves, G. D., and Spence, H. E.: Van Allen Probes measurements of energetic particle deep penetration into the low L region ($L < 4$) during the storm on 8 April 2016, *J. Geophys. Res.*, 122, 12140–12152, <https://doi.org/10.1002/2017JA024558>, 2017a.
- Zhao, H., Baker, D. N., Jaynes, A. N., Li, X., Elkington, S. R., Kanekal, S. G., Spence, H. E., Boyd, A. J., Huang, C.-L., and Forsyth, C.: On the relation between radiation belt electrons and solar wind parameters/geomagnetic indices: Dependence on the first adiabatic invariant and L^* , *J. Geophys. Res. Space Physics*, 122, 1624–1642, <https://doi.org/10.1002/2016JA023658>, 2017b.
- Wang, B., Nishimura, Y., Heitala, H., Lyons, L., Angelopoulos, V., Plaschke, F., Ebihara, Y., and Weatherwax, A.: Impacts of magnetosheath high-speed jets on the magnetosphere and ionosphere measured by optical imaging and satellite observations, *J. Geophys. Res. Space Physics*, 123, 4879–4894, <https://doi.org/10.1002/2017JA024954>, 2018.

Table 1 *FEE Enhancements observed by POES satellites*

FEE ID #	POES s/c ID	Observed time hh:mm UT	Longitude deg	LT* h
F1	P8	12:50	-164.2	1.8
F2	P5	13:15	-128.8	5.1
F3	P6	13:53	-138.3	5.1
F4	P8	14:32	169.7	1.6
F5	P5	14:54	-152.7	5.1
F6	P6	15:34	-162.5	5.0
F7	P2	15:44	-98.7	9.3
F8	P5	16:33	-170.1	5.0
F9	P7	16:37	-107.3	9.7
F10	P6	17:12	180.0	4.9
F11	P2	17:24	-123.0	9.4
F12	P7	18:16	-131.0	9.8
F13	P2	19:06	-140.0	9.6
F14	P8	20:30	-105.0	13.8
F15	P6	23:09	-94.5	17.2

* Local time

Table 2 *Timing of Magnetic Field Enhancements and Plasma Pulses from THEMIS and GOES12*

ID #	s/c ID	UT of magnetic peak hhmm:ss	UT of TH-D magnetosheath jet hhmm:ss	UT of TH-C foreshock pressure pulse hhmm:ss
1	TH-D	1333:40		~1328
	TH-E	1333:40		
	TH-B	1333:40		
	G12	1335:40		
2	TH-D	1420:50		~1417
	TH-E	1420:50		
	TH-B	1420:50		
	G12	1420:50		
3	TH-D	1550:30		~1549
	TH-E	1547:30		~1533, 1538
	G12	1544:00		
4	TH-D	1614:05	~1615 - 1616	~1611
	TH-E	1614:05		
	G12	1614:00		
5	TH-D	1638:20	~1640	~1634, 1636
	TH-E	1638:40		
	G12	1639:00		
6	TH-D	1647:45	~1648	absent
	TH-E	1647:45		
	G12	1648:00		
7	TH-D	-	~1651:30	absent
	TH-E	-		
8	TH-D	magnetosheath	~1700:30	~1700
	TH-E	-		
9	TH-D	magnetosheath	~1712 - 1713	~1707
	TH-E	1712:30		
10	TH-D	1722:30	~1725	~1718
	TH-E	1722:30		
	G12	1722:30		

Table 3*Location of Magnetic Stations in Geographic and Geomagnetic coordinates*

Code	Name	GLat ^a	GLon ^a	MLat ^b	MLon ^b
AAE	Addis Ababa	9.0	38.8	5.3	109.9
ABG	Alibag	18.6	72.9	9.5	144.4
ASC	Ascension Island	-8.0	-14.4	-1.4	54.7
ASP	Alice Springs	-23.8	133.9	-34.1	-153.6
BNG	Bangui	4.3	18.6	4.6	89.3
CMO	College	64.9	-147.9	64.8	-102.6
CNB	Canberra	-35.3	149.4	-43.8	-134.5
CTA	Charters Towers	-20.1	146.3	-29.1	-140.7
EYR	Eyrewell	-43.4	172.4	-47.8	-107.0
GUA	Guam	13.6	144.9	4.2	-146.3
GZH	Zhaoqing	23.0	112.5	11.7	-177.1
HON	Honolulu	21.3	-158.0	21.2	-92.7
KAK	Kakioka	36.2	140.2	26.2	-153.3
KDU	Kakadu	-12.7	132.5	-23.2	-156.3
KNY	Kanoya	31.4	130.9	20.7	-161.2
KOU	Kourou	5.2	-52.7	16.1	17.7
MBO	Mbour	14.4	-17.0	21.1	55.8
MCQ	McQuarie Island	-54.5	159.0	-60.9	-116.2
MMB	Memambetsu	43.9	144.2	34.2	-150.9
PET	Paratunka	53.0	158.3	45.6	-138.5
PHU	Phuthuy	21.0	106.0	9.7	176.0
PPT	Pamatai	-17.6	-149.6	-15.2	-76.5
SHU	Shumagin	55.4	199.5	54.1	-103.1
SIT	Sitka	57.1	-135.3	60.1	-83.7
TSU	Tsumeb	-19.2	17.6	-18.3	83.5
VSS	Vassouras	-22.4	-43.7	-12.1	24.6

^a Geographic latitude and longitude^b Magnetic latitude and longitude

FIGURE CAPTIONS

Figure 1. Geographic distribution of >30 keV electron fluxes measured by five NOAA/POES satellites on August 1, 2008 for the time interval (a) 0-12 UT, before the electron flux enhancements and (b) 12-24 UT, during the enhancements. The electrons are detected in vertical direction. In the forbidden zone those electrons are quasi-trapped. The electron fluxes enhanced largely during nonstorm condition after 12 UT. The forbidden zone is bounded by $L=1.2$ (white lines) and located outside of the South Atlantic Anomaly (SAA) at equatorial-to-low latitudes. Drift L-shells are calculated from IGRF-2005 model. The solid black curve indicates the dip equator.

Figure 2. FEE enhancements on 1 August 2008: (a) fluxes of >30 keV electrons in units $(\text{cm}^2 \text{ s sr})^{-1}$, (b) L-shell of enhancements, (c) longitude and (d) local time of peak fluxes (black circles). Measurements within the SAA area are indicated by the open circles. Colorful curves denote NOAA/POES satellites: P2 (black), P5 (pink), P6 (red), P7 (blue), and P8 (green). Horizontal dashed line at panel (b) depicts the lower edge of the inner radiation belt. FEE enhancements peak at the equator (minimal L-shells) that indicates a fast radial transport from the inner radiation belt.

Figure 3. Solar wind parameters from OMNI data and geomagnetic indices on August 1, 2008. From top to bottom: (a) solar wind density (black) and dynamic pressure (blue), (b) solar wind speed, (c) interplanetary magnetic field (IMF) components B_x (blue), B_y (green), B_z (red) and magnitude B (black) in Geocentric Solar Magnetospheric (GSM) coordinates, (d) polar cap magnetic activity index PCN for northern (blue) and PCS for southern (red) hemispheres, (e) auroral electrojet index AE (black), AL (red), AU (green), and (f) storm time ring current variation index SYM-H. The shaded box denotes the time interval from 13 to 23 UT, when the nonstorm FEE enhancements were observed.

Figure 4. Spacecraft positions in GSM coordinates from 1200 to 1800 UT on August 1, 2008. The TH-C probe (blue) was in front of the subsolar bow shock. The TH-E (orange), TH-D (green), TH-B (brown), and GOES 12 (black) were located inside the dayside magnetosphere. The magnetopause position (black curve) was calculated using OMNI data for the upstream conditions at ~ 1600 UT following the model by Lin et al.'s (2010).

Figure 5. Observations of plasma and magnetic field on August 1, 2008. (a) Ion spectrogram (ion flux is in units of $\text{eV}/\text{cm}^2 \text{ s sr eV}$) and IMF vector components in GSM coordinates measured by TH-C, (b) IMF vector components from OMNI data set. Comparison of OMNI and TH-C data: (c) IMF cone angles plotted for OMNI (black) and TH-C (pink), red curve shows TH-C smoothed cone

angle. (d) Solar wind dynamic pressure for OMNI (black circle), ACE (blue curve) and for TH-C (red curve). Grey curve shows TH-C total pressure (sum of dynamic, magnetic and thermal pressures). The ACE data are shifted by 60 min.

Figure 6. Satellite measurements of magnetic field and plasma in the dayside magnetosphere and geomagnetic activity. (a) The B_z -GSM components from THEMIS probes TH-B (brown), TH-E (orange), and TH-D (green). The left y-axis corresponds to the magnetic measurements from TH-B and TH-D, and the right y-axis to TH-E. (b) The detrended magnetic fields for THEMIS. (c) The GOES-12 (black) and GOES-10 (blue) measurements of magnetic field strength (left y-axis) and local time (right y-axis). (d) The SYM-H index; and (e) the ion spectrogram from TH-D (ion flux is in units of $\text{eV}/\text{cm}^2 \text{ s sr eV}$). Dashed lines, numbered from 1 to 10, indicate magnetic and plasma disturbances observed by THEMIS.

Figure 7. Observations of plasma and magnetic field at 1530-1800 UT on August 1, 2008: (a,b) ion spectrograms measured by TH-C, TH-D (ion flux is in units of $\text{eV}/\text{cm}^2 \text{ s sr eV}$), (c) horizontal magnetic field H_p detected by GOES 12 from 10 to 13 LT, (d) magnetic field strengths B_{tot} from TH-D (green) and TH-E (red), (e) IMF cone angles for TH-C (black) and for the ACE upstream monitor (blue). (f) TH-C solar wind dynamic pressure. Dashed lines and numbers 4 - 10 mark plasma structures of magnetosheath ions observed inside the magnetosphere.

Figure 8. Observations of plasma and magnetic field during the intervals 1600 - 1630 UT, 1630 - 1700 UT and 1658 - 1728 UT on August 1, 2008. Panels show from top to bottom: (a) ion spectrogram from TH-D, (b) total pressure P_{tot} measured by the ACE upstream monitor (black) and TH-D (red), (c) plasma density D measured by ACE (black) and TH-D (blue), (d) TH-D measurements of bulk velocity V (black) and its components in GSM coordinates V_x (blue), V_y (green) and V_z (red), (e) transversal components of magnetic field B_x (blue) and B_y (green) from TH-D, (f) magnitude B and B_z component of magnetic field from TH-D, (g) magnitude B and B_z component of magnetic field from TH-E. The magnetosheath plasma penetration is denoted by dashed lines and numbers #4 - #10.

Figure 9. Relative variations in the horizontal component (H) of the geomagnetic field at low geomagnetic latitudes. Local time intervals are indicated near the station codes. The vertical lines depict magnetic peaks #1 - #3 at THEMIS (see Table 2). Bottom panel shows magnetic field B measured by GOES-12 (black) and detrended magnetic field from TH-D (green).

Figure 10. Relative variations in the horizontal component (H) of the geomagnetic field in the midnight (left) and predawn (right) sectors. The geomagnetic latitudes of the stations are indicated near station codes. The vertical lines depict magnetic peaks at THEMIS (see Table 2). Magnetic data from THEMIS and GOES satellites are shown at lower panels on the right.

Figure 11. Dynamics of the geomagnetic field and particles on 1 August 2008: (a) FEE enhancements, (b) plasma precipitation at high latitudes, and dayside magnetic field perturbations observed by (c) GOES-12 (black), TH-D (green) and TH-B (brown). The left y-axis corresponds to GOES-12, and the right y-axis to TH-D and TH-B. The numbers indicate the FEE injections at ~2 and ~5 LT (see Table 1), colors for POES satellite are the same as in Figure 2. Plasma precipitations are shown for the energy flux above the threshold of 0.5 (erg/sm² s) and are grouped in LT: 23 – 24 LT (light gray), 0 – 2 LT (gray), 5 – 6 LT (blue), 12.5 - 15 LT (red points), 15 – 16 LT (violet), and 19.5 – 21.5 LT (green).

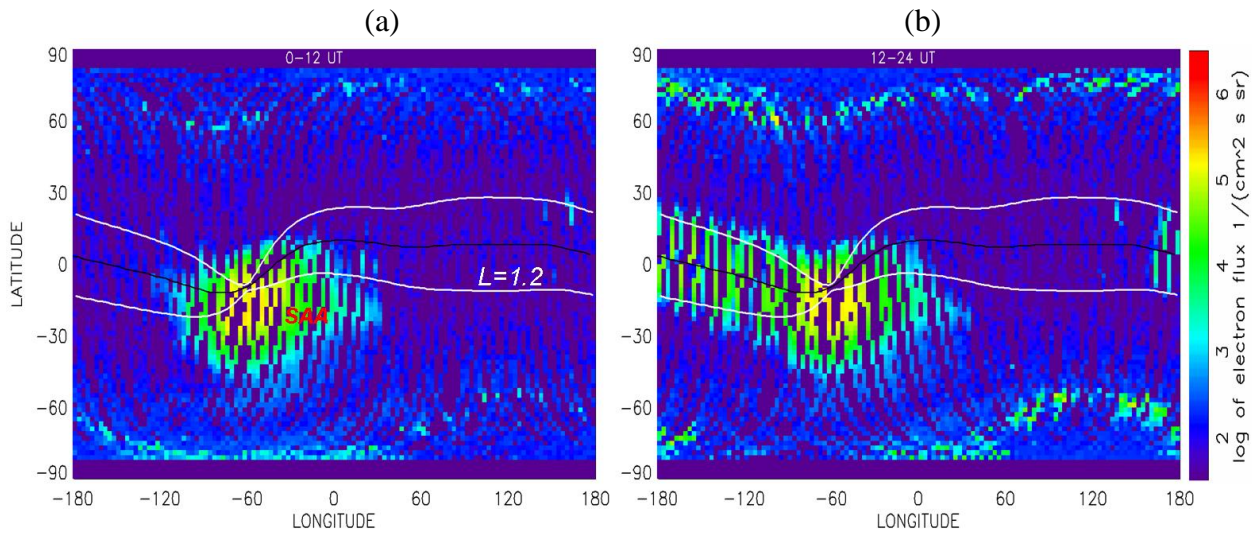


Figure 1. Geographic distribution of >30 keV electron fluxes measured by five NOAA/POES satellites on August 1, 2008 for the time interval (a) 0-12 UT, before the electron flux enhancements and (b) 12-24 UT, during the enhancements. The electrons are detected in vertical direction. In the forbidden zone those electrons are quasi-trapped. The electron fluxes enhanced largely during nonstorm condition after 12 UT. The forbidden zone is bounded by $L=1.2$ (white lines) and located outside of the South Atlantic Anomaly (SAA) at equatorial-to-low latitudes. Drift L-shells are calculated from IGRF-2005 model. The solid black curve indicates the dip equator. The

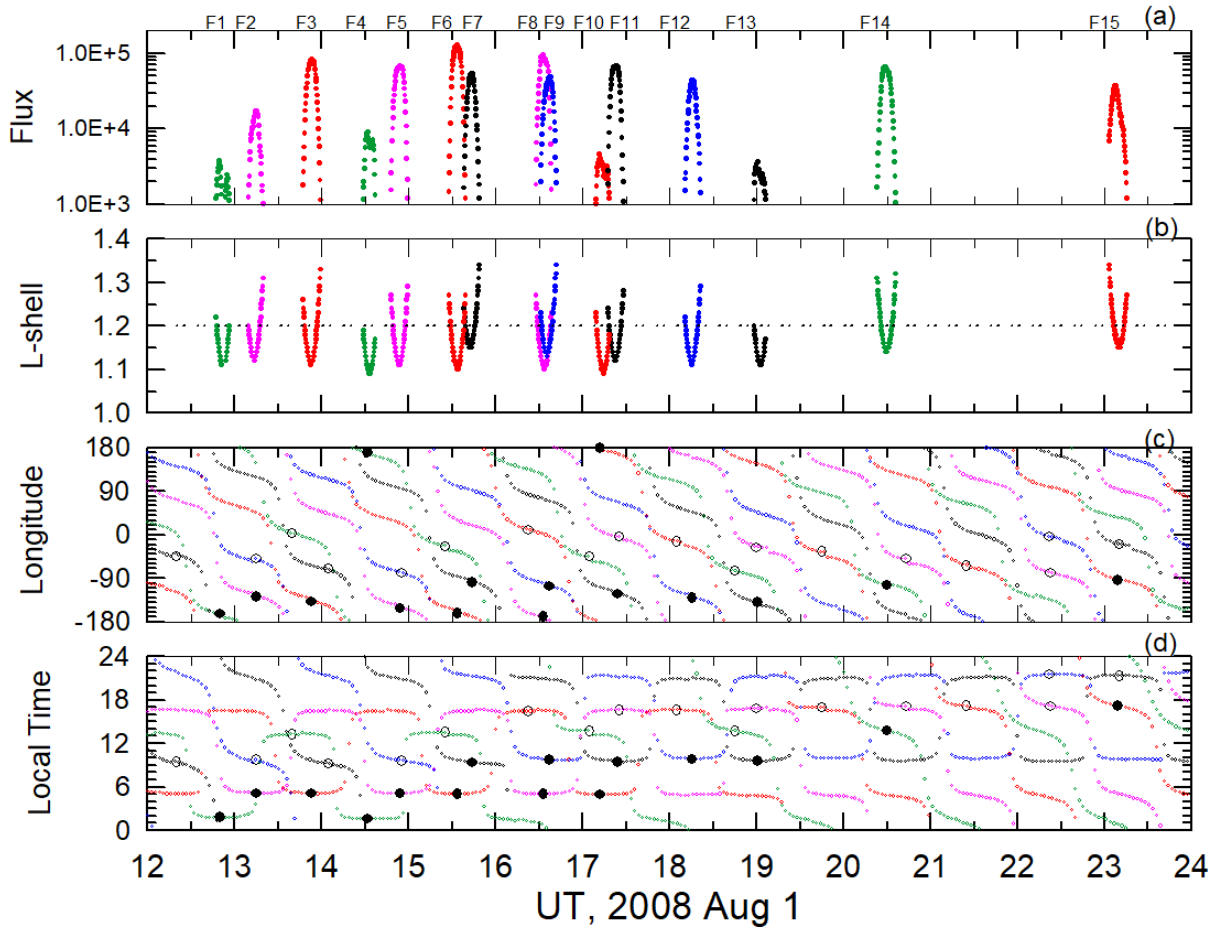


Figure 2. FEE enhancements on 1 August 2008: (a) fluxes of >30 keV electrons in units $(\text{cm}^2 \text{ s sr})^{-1}$, (b) L-shell of enhancements, (c) longitude and (d) local time of peak fluxes (black circles). Measurements within the SAA area are indicated by the open circles. Colorful curves denote NOAA/POES satellites: P2 (black), P5 (pink), P6 (red), P7 (blue), and P8 (green). Horizontal dashed line at panel (b) depicts the lower edge of the inner radiation belt. FEE enhancements peak at the equator (minimal L-shells) that indicates a fast radial transport from the inner radiation belt.

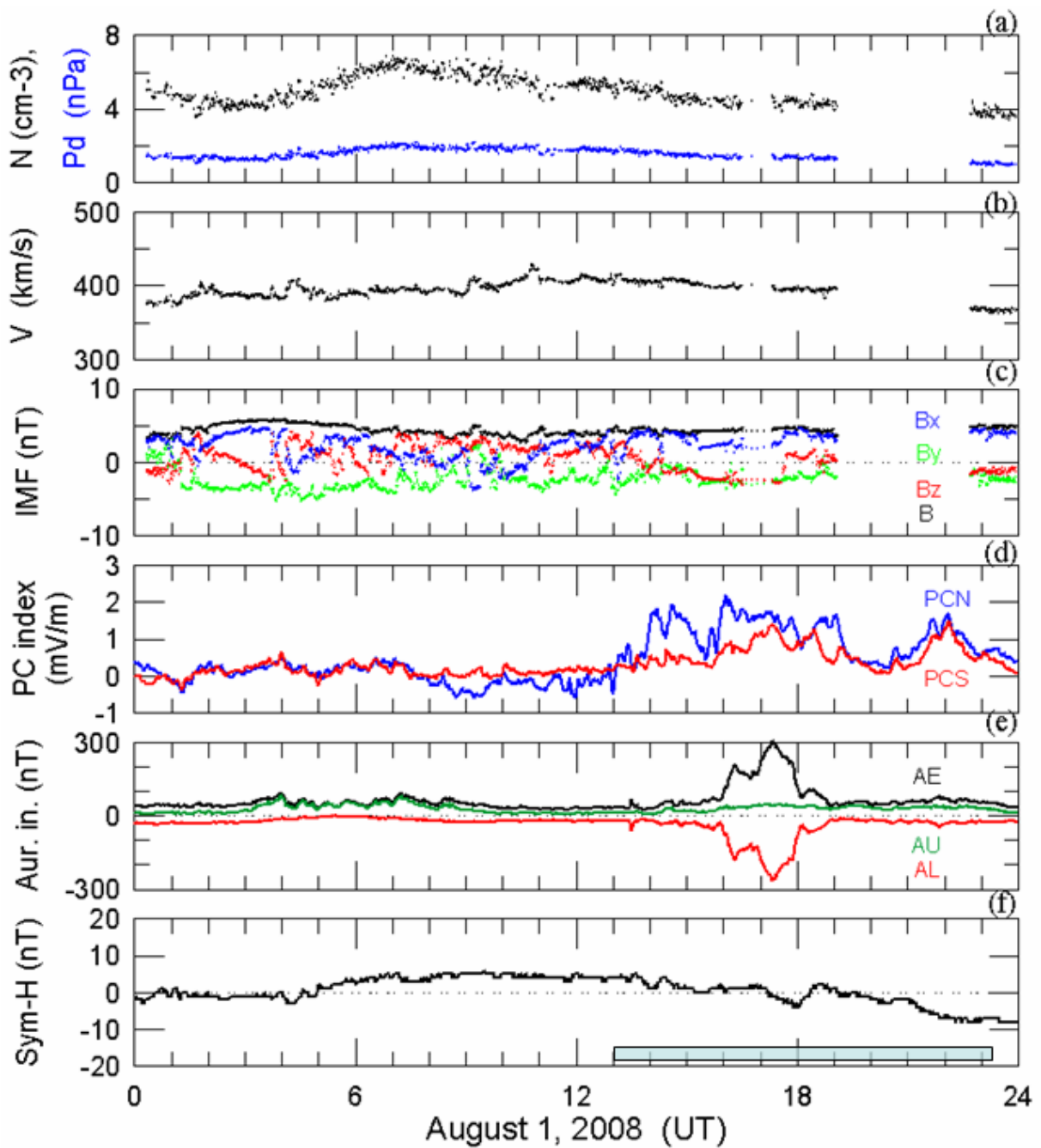


Figure 3. Solar wind parameters from OMNI data and geomagnetic indices on August 1, 2008. From top to bottom: (a) solar wind density (black) and dynamic pressure (blue), (b) solar wind speed, (c) interplanetary magnetic field (IMF) components Bx (blue), By (green), Bz (red) and magnitude B (black) in Geocentric Solar Magnetospheric (GMS) coordinates, (d) polar cap magnetic activity index PCN for northern (blue) and PCS for southern (red) hemispheres, (e) auroral electrojet index AE (black), AL (red), AU (green), and (f) storm time ring current variation index

SYM-H. The shaded box denotes the time interval from 13 to 23 UT, when the nonstorm FEE enhancements were observed.

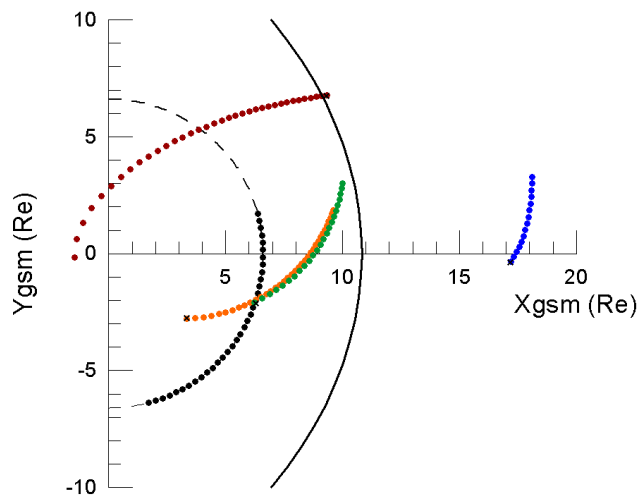


Figure 4. Spacecraft positions in GSM coordinates from 1200 to 1800 UT on August 1, 2018. The TH-C probe (blue) was in front of the subsolar bow shock. The TH-E (orange), TH-D (green), TH-B (brown), and GOES 12 (black) were located inside the dayside magnetosphere. The magnetopause position (black curve) was calculated using OMNI data for the upstream conditions at ~1600 UT following the model by Lin et al.'s (2010).

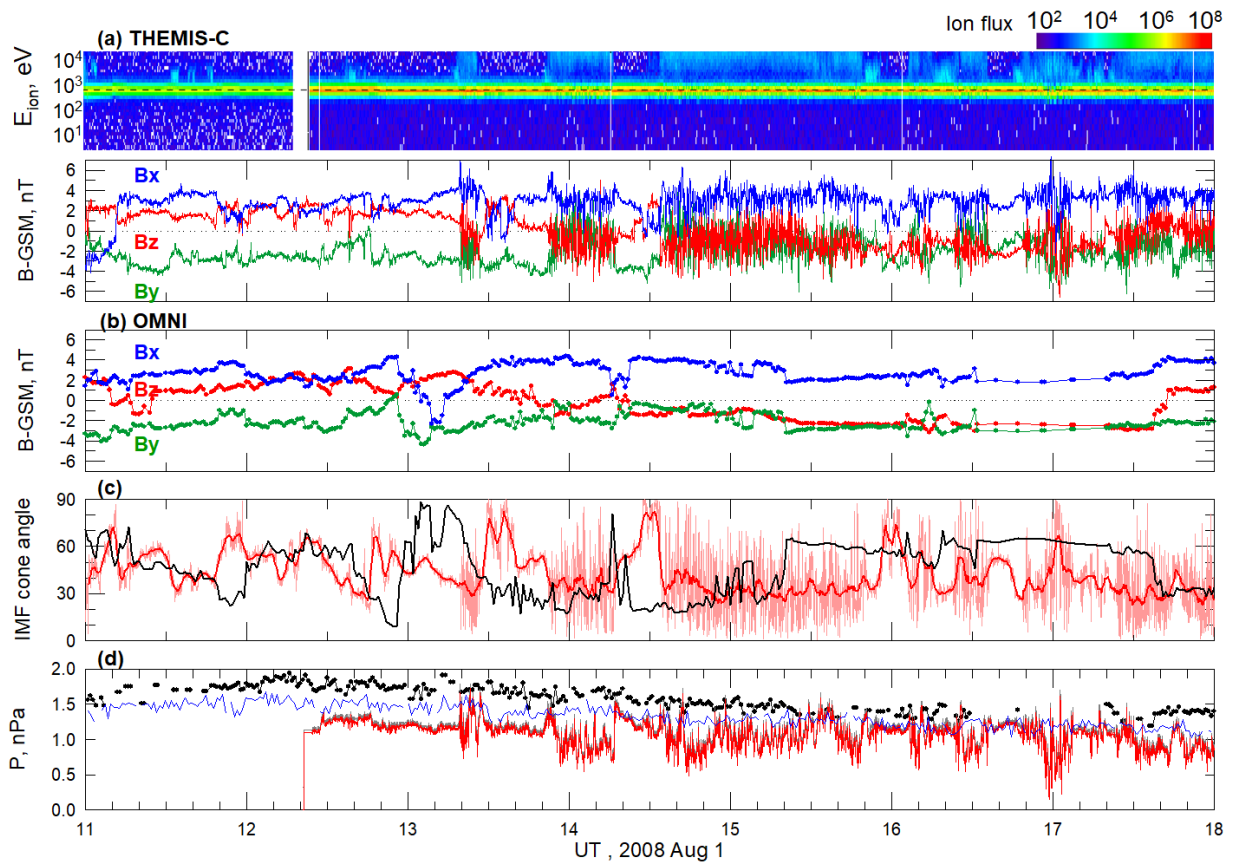


Figure 5. Observations of plasma and magnetic field on August 1, 2008. (a) Ion spectrogram (ion flux is in units of eV/cm² s sr eV) and IMF vector components in GSM coordinates measured by TH-C, (b) IMF vector components from OMNI data set. Comparison of OMNI and TH-C data: (c) IMF cone angles plotted for OMNI (black) and TH-C (pink), red curve shows TH-C smoothed cone angle. (d) Solar wind dynamic pressure for OMNI (black circle), ACE (blue curve) and for TH-C (red curve). Grey curve shows TH-C total pressure (sum of dynamic, magnetic and thermal pressures). The ACE data are shifted by 60 min.

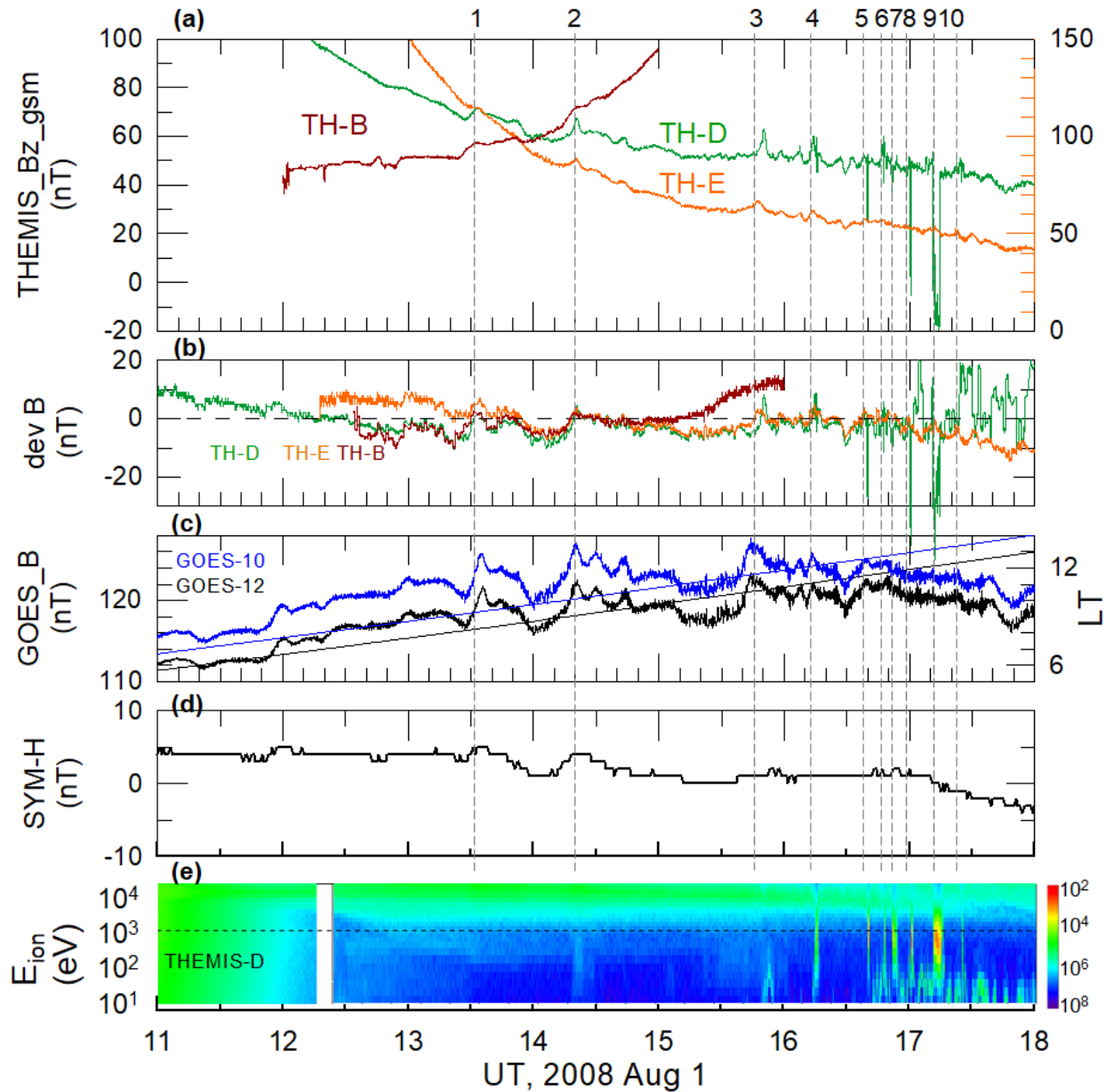


Figure 6. Satellite measurements of magnetic field and plasma in the dayside magnetosphere and geomagnetic activity. (a) The B_z -GSM components from THEMIS probes TH-B (brown), TH-E (orange), and TH-D (green). The left y-axis corresponds to the magnetic measurements from TH-B and TH-D, and the right y-axis to TH-E. (b) The detrended magnetic fields for THEMIS. (c) The GOES-12 (black) and GOES-10 (blue) measurements of magnetic field strength (left y-axis) and local time (right y-axis). (d) The SYM-H index; and (e) the ion spectrogram from TH-D (ion flux is in units of $\text{eV}/\text{cm}^2 \text{ s sr eV}$). Dashed lines, numbered from 1 to 10, indicate magnetic and plasma disturbances observed by THEMIS.

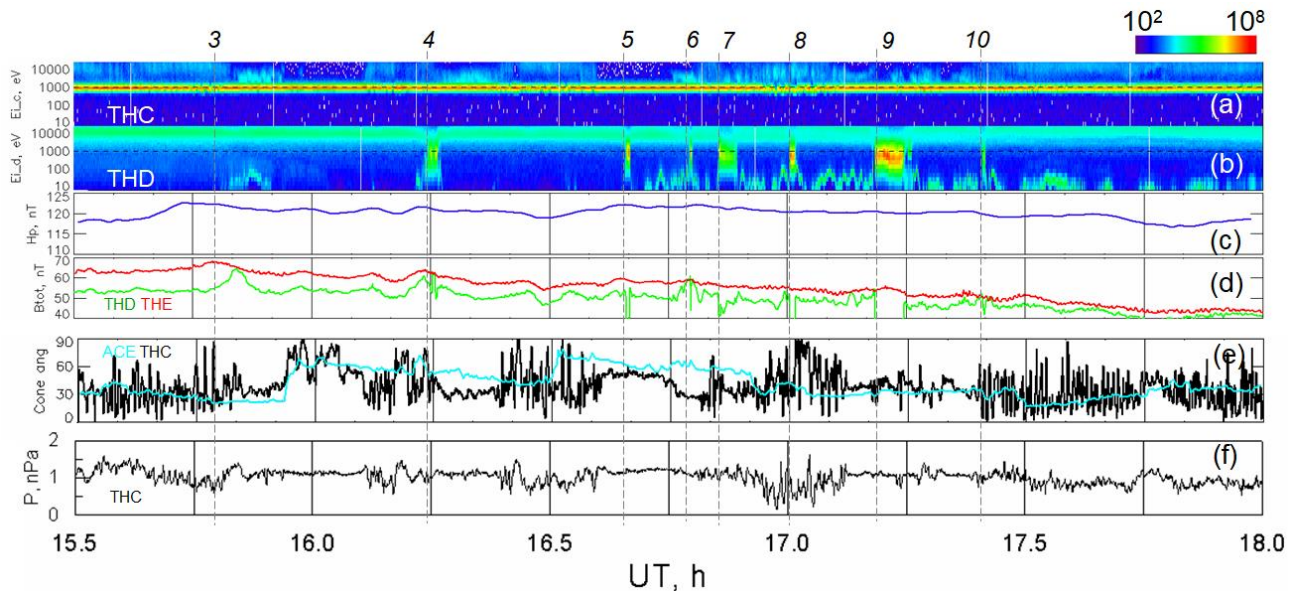


Figure 7. Observations of plasma and magnetic field at 1530-1800 UT on August 1, 2008: (a,b) ion spectrograms measured by TH-C, TH-D (ion flux is in units of $\text{eV}/\text{cm}^2 \text{ s sr eV}$), (c) horizontal magnetic field H_p detected by GOES 12 from 10 to 13 LT, (d) magnetic field strengths B_{tot} from TH-D (green) and TH-E (red), (e) IMF cone angles for TH-C (black) and for the ACE upstream monitor (blue). (f) TH-C solar wind dynamic pressure. Dashed lines and numbers 4 - 10 mark plasma structures of magnetosheath ions observed inside the magnetosphere.

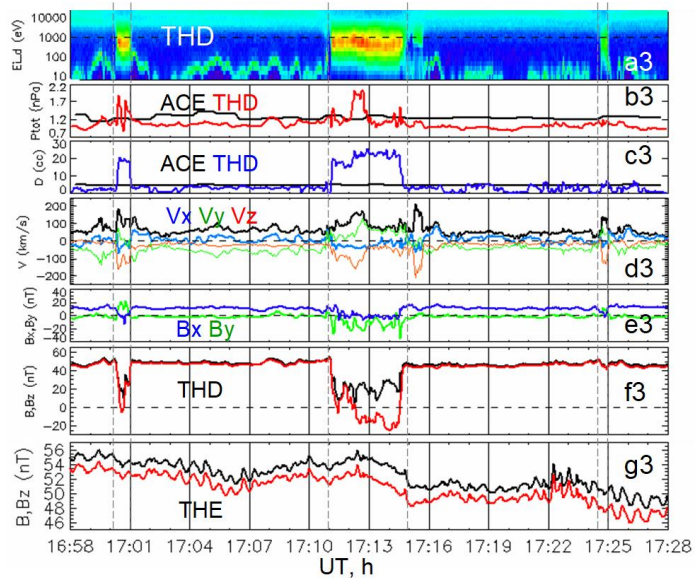
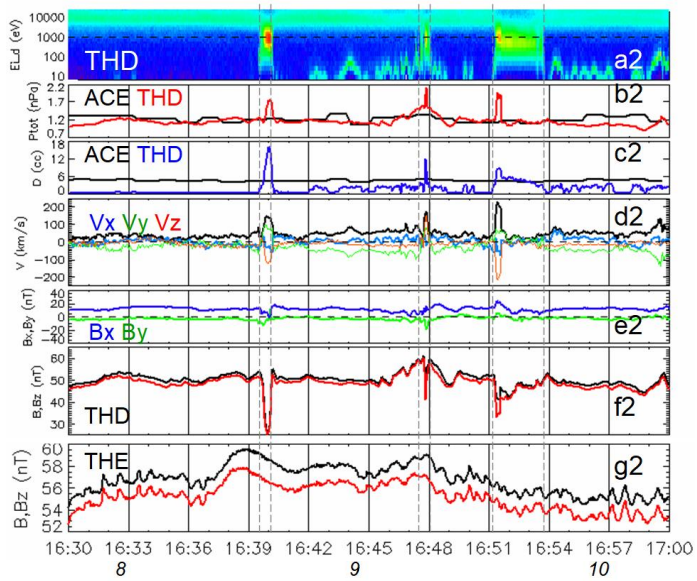
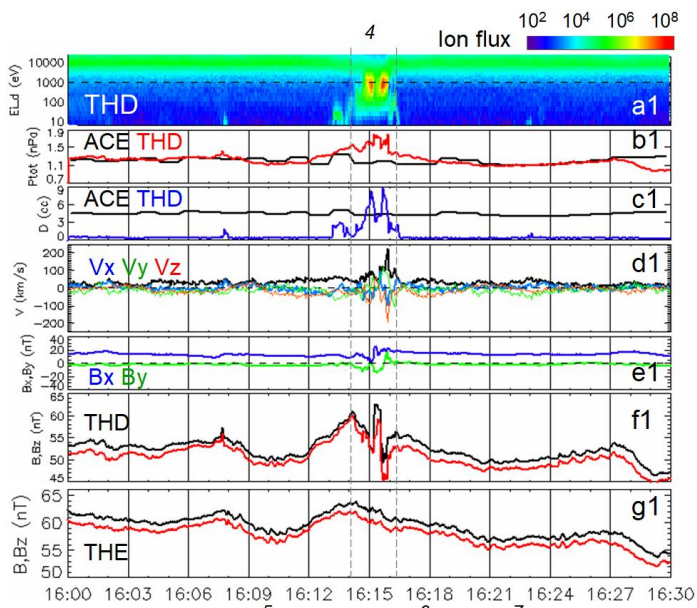


Figure 8. Observations of plasma and magnetic field during the intervals 1600 - 1630 UT, 1630 - 1700 UT and 1658 - 1728 UT on August 1, 2008. Panels show from top to bottom: (a) ion spectrogram from TH-D, (b) total pressure measured by the ACE upstream monitor (black) and TH-D (red), (c) plasma density measured by ACE (black) and TH-D (blue), (d) TH-D measurements of bulk velocity V (black) and its components in GSM coordinates V_x (blue), V_y (green) and V_z (red), (e) transversal components of magnetic field B_x (blue) and B_y (green) from TH-D, (f) magnitude B and B_z component of magnetic field from TH-D, (g) magnitude B and B_z component of magnetic field from TH-E. The magnetosheath plasma penetration is denoted by dashed lines and numbers #4 - #10.

Equator – to – Low latitudes

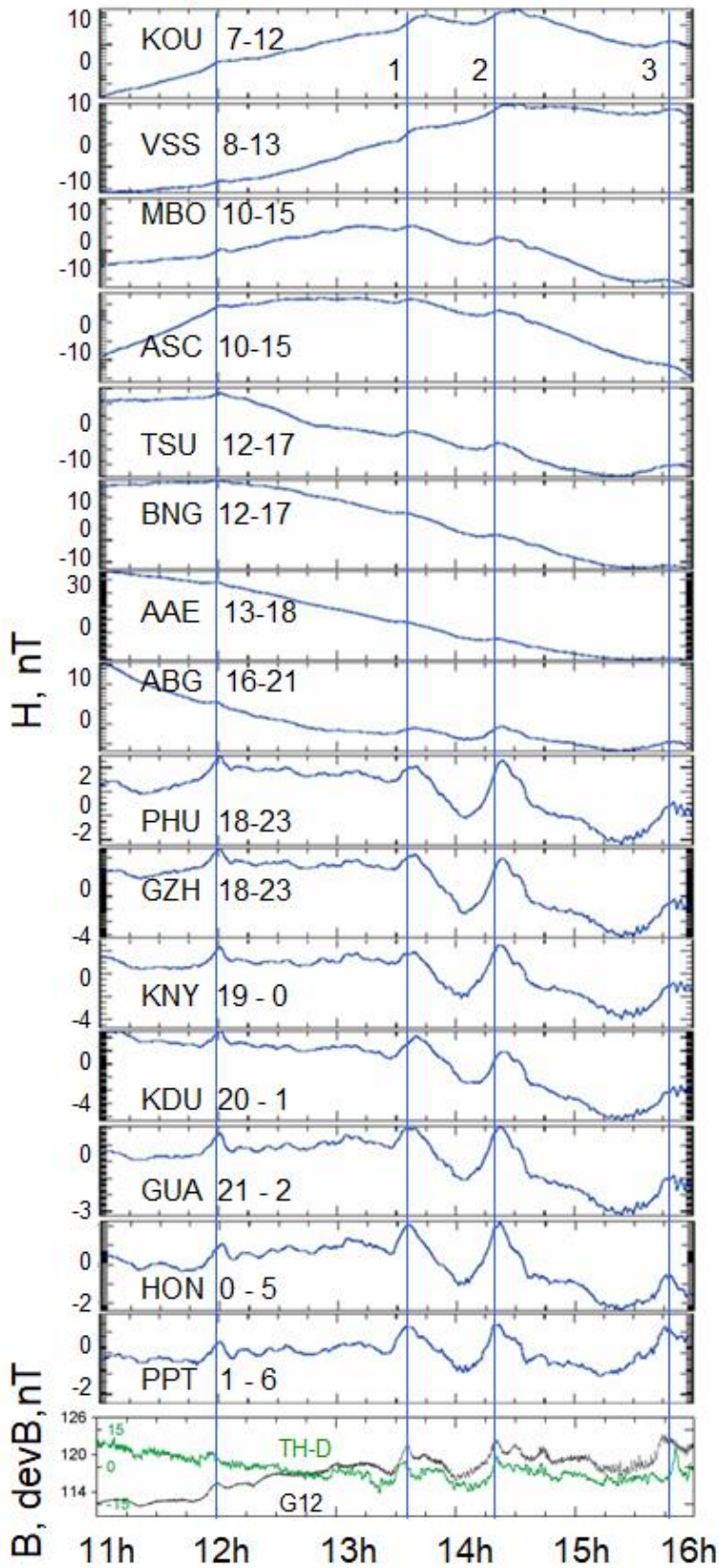


Figure 9. Relative variations in the horizontal component (H) of the geomagnetic field at low geomagnetic latitudes. Local time intervals are indicated near the station codes. The vertical lines depict magnetic peaks #1 - #3 at THEMIS (see Table 2). Bottom panel shows magnetic field B measured by GOES-12 (black) and detrended magnetic field from TH-D (green).

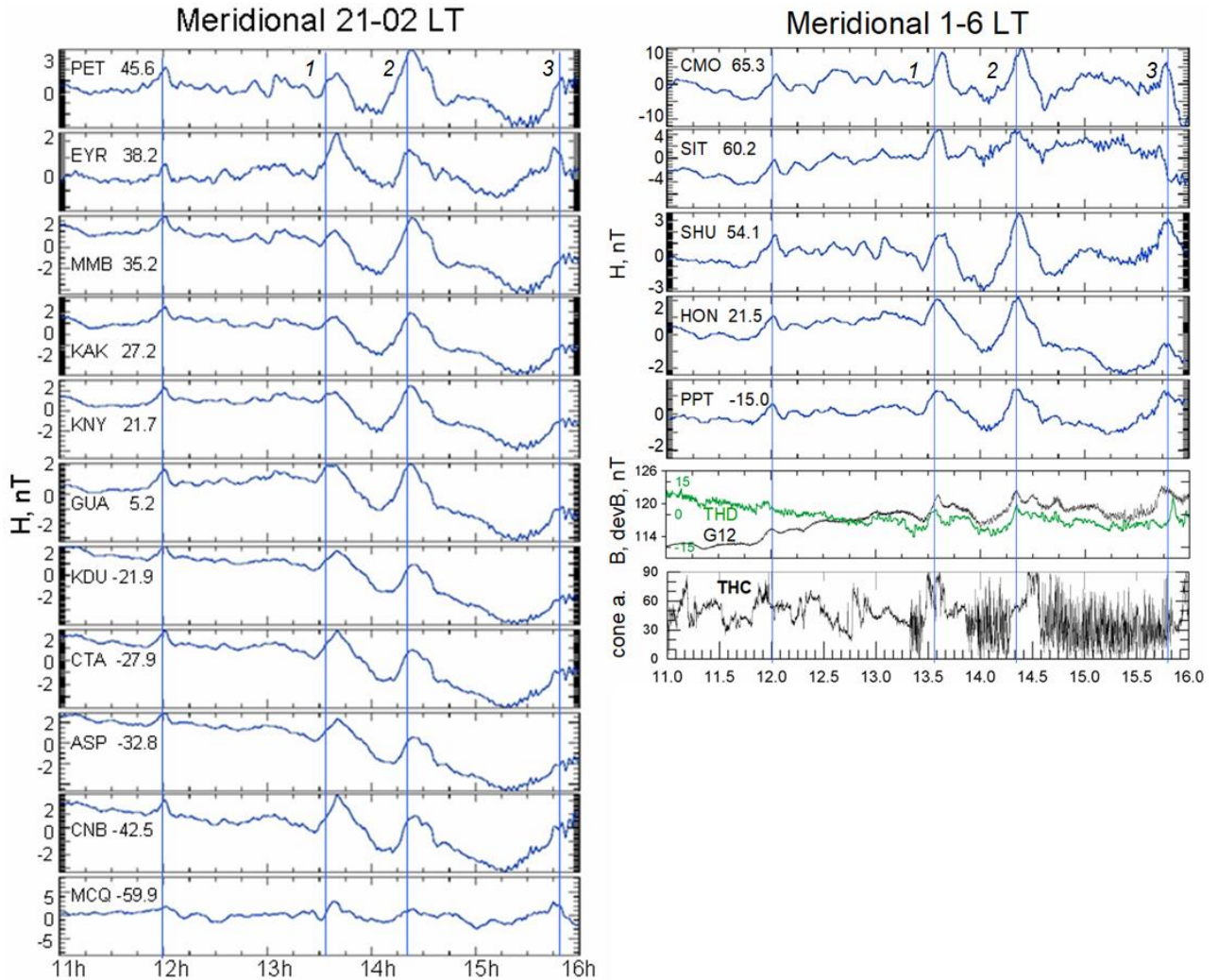


Figure 10. Relative variations in the horizontal component (H) of the geomagnetic field in the midnight (left) and predawn (right) sectors. The geomagnetic latitudes of the stations are indicated near station codes. The vertical lines depict magnetic peaks at THEMIS (see Table 2). Magnetic data from THEMIS and GOES satellites are shown at lower panels on the right.

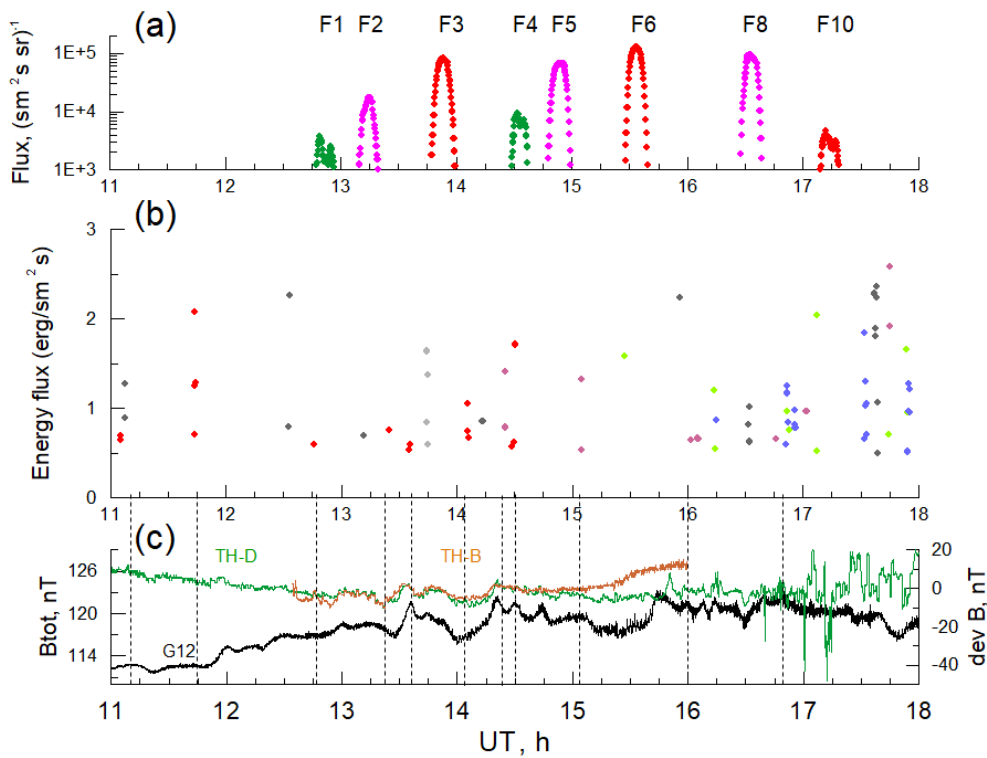


Figure 11. Dynamics of the geomagnetic field and particles on 1 August 2008: (a) FEE enhancements, (b) plasma precipitation at high latitudes, and dayside magnetic field perturbations observed by (c) GOES-12 (black), TH-D (green) and TH-B (brown). The left y-axis corresponds to GOES-12, and the right y-axis to TH-D and TH-B. The numbers indicate the FEE injections at ~ 2 and ~ 5 LT (see Table 1), colors for POES satellite are the same as in Figure 2. Plasma precipitations are shown for the energy flux above the threshold of $0.5 \text{ (erg}/\text{sm}^2 \text{ s)}$ and are grouped in LT: 23 – 24 LT (light gray), 0 – 2 LT (gray), 5 – 6 LT (blue), 12.5 - 15 LT (red points), 15 – 16 LT (violet), and 19.5 – 21.5 LT (green).